

Morphology of P3HT in Thin Films in Relation to Optical and Electrical Properties

Kim Tremel and Sabine Ludwigs

Abstract The search for renewable and environmentally friendly energy sources has made organic electronics an interesting field of research. Semiconducting polymers stand out because they offer cheap and easy processability at a large-scale from solution, combined with impressive optoelectronic properties. Polythiophenes, in particular poly(3-hexylthiophene) (P3HT), are the most prominent and investigated representatives of semiconducting polymers and have been applied in various devices such as solar cells and field-effect transistors. For this class of polymers, it has been well established that the morphology of the functional layer has a significant impact on the device performance. However, transport bottlenecks are hard to determine due to the complex semicrystalline microstructure, which is composed of a mixture of crystalline and amorphous domains. In order to gain a deeper understanding of the correlation between microstructure and functional properties, precise control of nucleation and growth of semicrystalline polymers such as P3HT is crucial. This article gives an overview of recent publications addressing the morphology and crystallization of regioregular P3HT, both in solution and thin film, and attempts to correlate these structural features to the functional (i.e. optical and electrical) properties of the polymer.

Keywords Absorption behavior • Charge transport • Crystallization • Nanostructure • Ordered nanostructure • Poly(3-hexylthiophene)

K. Tremel and S. Ludwigs (✉)
IPOC-Functional Polymers, Institute of Polymer Chemistry, University of Stuttgart,
Pfaffenwaldring 55, 70569 Stuttgart, Germany
e-mail: sabine.ludwigs@ipoc.uni-stuttgart.de

Contents

1	Introduction	40
2	Regioregular Poly(3-hexylthiophene): Functional Properties	41
2.1	Materials	41
2.2	Energy Levels from Electrochemical Measurements	43
2.3	Optical Properties of P3HT Solutions	45
3	Crystallization from Solution	47
4	Thin Film Properties	52
4.1	Preparation and Characterization of P3HT Films	54
4.2	Inducing Order and Orientation in P3HT Thin Films	67
5	Conclusions	78
	References	78

1 Introduction

Semiconducting polymers have attracted a great deal of attention in the last decades because of their remarkable optoelectronic properties combined with low-cost solution processability [1–4]. One of the most prominent semiconducting polymers is poly(3-hexylthiophene) (P3HT), whose optoelectronic properties and device performance have been investigated extensively in numerous studies [1, 5–7]. Most of the fascinating properties of semiconducting polymers such as P3HT derive from their strong tendency to crystallize, because strong intermolecular interactions in well-ordered crystalline domains offer efficient charge transport pathways through the polymer layer on a macroscopic scale [8]. Polymer crystallization of flexible chains such as polyethylene (PE) has been described by numerous theories [9, 10]. As a result of different processing conditions, there is a great diversity of morphologies for these polymers, which have been widely explored and reviewed [11] during the last 50 years. Crystalline lamellae based on folded chains are unique for polymer crystals. Lamellae can further aggregate and form semicrystalline spherulites under static conditions, whereas an external field provokes anisotropic structures such as polymer fibrils [12, 13]. Precise control of crystallization conditions can allow the growth of single crystals [14, 15] formed of folded-chain lamellae, which are not only used for investigations of the crystallographic structure, but also for exploring crystallization kinetics. From an engineering point of view, the precise morphology is of great relevance because the mechanical properties strongly depend on the microstructure. Crystallization of conjugated polymers like P3HT is more complex due to the rigidity of the polymer backbone and the presence of side chains, which follow distinct crystallization kinetics [16]. A precise crystallization mechanism for conjugated polymers has not yet been fully established. The great advantage of a conjugated polymer backbone, however, is that it allows for functional properties with a characteristic absorption in the low-energy part of the spectrum and highly anisotropic charge transport. Hence, the exact morphology affects not only the mechanical but also the functional properties of the polymer layer and is therefore

crucial for device performance. For instance, charge transport is highly dependent on the order within the polymer layer at multiple length scales: On a local scale, charge transfer is affected by the extent of π -conjugation along the backbone as well as intermolecular chain contacts. On a macroscopic scale, the interconnectivity of crystalline grains plays a crucial role in the charge carrier mobility. Therefore, improving device performance requires precise control of morphology, and new methods to manipulate and control the polymer microstructure are continuously pursued. From a research point of view, gaining a detailed understanding of the correlation between morphology and functional properties is challenging and has been the focus of various publications [1, 17–20].

This chapter gives an overview of recent reports on the control of morphology of regioregular P3HT in thin films. Starting from a short introductory section about synthesis, energy levels, and optical properties in solution, we then discuss the preparation of one-dimensional (1D) fibers by controlled crystallization from solution. We then focus on P3HT thin films obtained by solution processing from good solvents, a procedure that is highly relevant for large-scale applications. The impact of molecular parameters and processing conditions on the semicrystalline morphology of P3HT on substrates is discussed in this context. The last part of the chapter deals with the manufacture of oriented structures of P3HT with long range order, with the clear perspective of understanding structure–function relations.

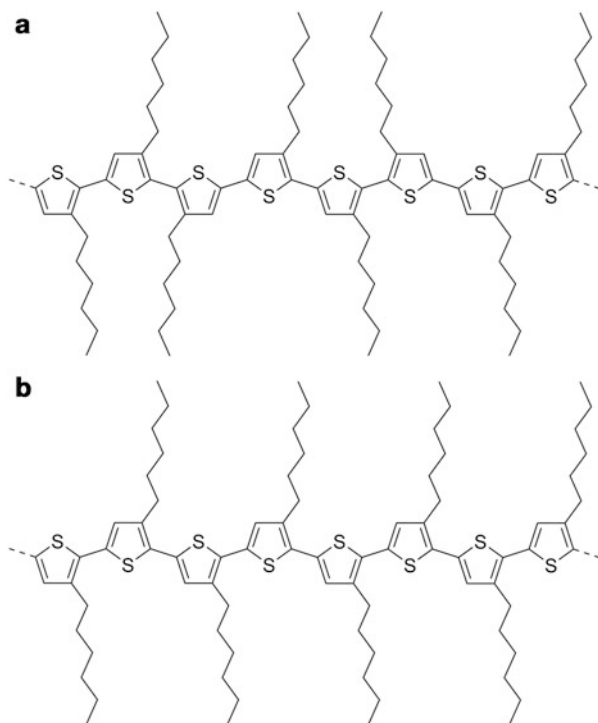
2 Regioregular Poly(3-hexylthiophene): Functional Properties

2.1 Materials

One of the first syntheses of unsubstituted polythiophenes with high conductivity after doping with iodine was reported in 1980 [21, 22]. However, due to the lack of processability of these polymers, alkyl chains were attached to the conjugated backbone to make the polymer soluble in common organic solvents and to allow deposition from solution. Because 3-alkylthiophene is an asymmetric monomer, there are three different regioisomers that vary in the relative orientation of the two thiophene rings when coupled between the 2- and 5-position: 2-2' or head-to-head coupling (HH), 2-5' or head-to-tail coupling (HT), and 5-5' or tail-to-tail coupling (TT).

As a result, polymers based on 3-alkylthiophene exhibit a different regiochemistry, which is illustrated in Fig. 1 for the example of P3HT. Polythiophenes containing a mixture of the different couplings are referred to as regiorregular or regiorandom. For polymers with irregular substituent distribution, the thiophene units twist away from planarity as a result of unfavorable HH coupling, which results in a drastic decrease in the conjugation length. In contrast, regioregular polythiophenes, which contain exclusively HT couplings, can adopt a

Fig. 1 Regioirregular (a) and regioregular (b) poly (3-hexylthiophene)



planar conformation of low energy with extended π -conjugation. This leads to highly desirable properties for device applications, such as effective charge transport and high absorption in the low energy part of the visible spectrum. In 1992, McCullough and Lowe described the first synthesis of regioregular P3HT via Ni-catalyzed Kumada cross-coupling [23, 24]. Using 3-alkylthiophene as the starting material, selective bromination to 2-bromo-3-alkylthiophene was followed by lithiation, transmetalation, and polymerization in the presence of nickel. In the same year, Chen and Rieke presented a second approach for the synthesis of regioregular P3HT via polycondensation of 2,5-dibromo-3-alkylthiophene using active zinc (“Rieke Zn”) and nickel catalysis [25]. Both methods presented a breakthrough for polymer electronics, giving regioregular poly(3-alkylthiophene)s (P3ATs) with high conductivity. However, synthesis at a large scale was problematic because of the low temperatures necessary during reaction. This problem was overcome in 1999 by McCullough, who reported the synthesis of highly regioregular P3ATs by the Grignard metathesis reaction (GRIM), which allows synthesis at room temperature and at a large scale [26]. Recent progress on defect-free polythiophenes with controlled terminal groups has been accomplished by external initiation, developed and extended by Kiriya and Luscombe, respectively [27, 28]. A detailed review of synthetic routes for regioregular P3HT, including mechanistic details, can be found in the chapter by Sista and Luscombe in this book [29].

The literature we review in this chapter deals mainly with polymers that are made by the standard polymerization routes and that are commercially available. To obtain P3HT with different molecular weights, the method of Soxhlet extraction is quite common, first demonstrated for regioregular P3HT by Trznadel et al. [30]. Soxhlet extraction makes use of the different quality of solvents to separate P3HT into fractions of better defined molecular weight with narrow molecular weight distribution. Throughout this review we have tried to specify the molecular weight and polydispersity index of the samples studied in the cited publications to make the studies as comparable as possible.

2.2 Energy Levels from Electrochemical Measurements

P3HT is a classical semiconducting polymer that is nonconducting in the neutral state and becomes conducting upon doping. Figure 2a schematically shows the process of oxidation or p-doping to radical-cationic/polaron species and the reduction or n-doping to radical-anionic/polaron species by chemical or electrochemical doping.

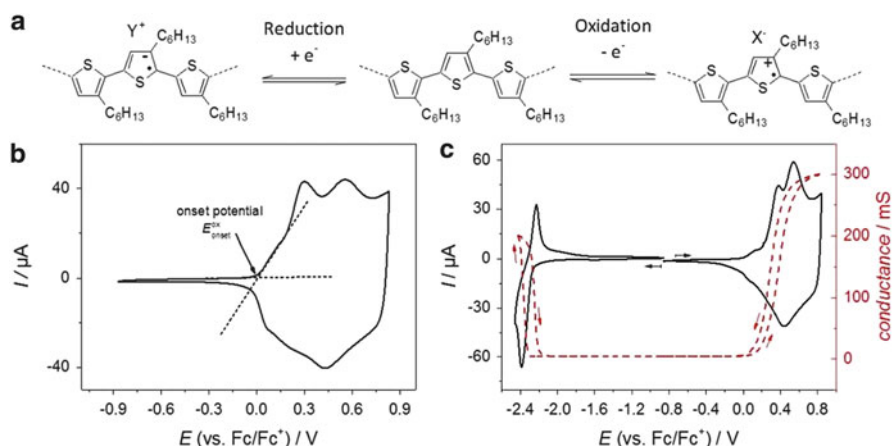


Fig. 2 (a) Molecular structure of the neutral (*middle*), reduced (*left*), and oxidized (*right*) forms of P3HT. The incorporation of counter ions (Y^+ , X^-) from the supporting electrolyte during the electrochemical doping process ensures electroneutrality within the charged film. (b) Method for the determination of the oxidation onset potential value of P3HT from a cyclic voltammogram of a P3HT film deposited on a Pt working electrode; $\nu = 50$ mV/s, electrolyte: 0.1 M TBAPF₆/MeCN. The interception of the two tangents (*dashed lines*) at the initial slope of the peak current corresponds to E_{onset}^{ox} . (c) Cyclic voltammograms (*black*) including in-situ conductance measurements (*red*) of the reduction (n-doping) and oxidation (p-doping) of a P3HT film deposited on a Pt working electrode; $\nu = 20$ mV/s, electrolyte: 0.1 M TBAPF₆/MeCN; oxidation and reduction were recorded separately; *arrows* indicate scan direction. (Data measured by M. Goll and Dr. A. Ruff)

Determination of the energy levels is typically performed by electrochemistry, and cyclic voltammetry (CV) has been established as method of choice. The polymer is either dissolved in the supporting electrolyte or deposited on the working electrode. The measurements are usually performed with a three-electrode set-up that includes a working electrode, a reference electrode (for example Ag/AgCl), and a counter or auxiliary electrode. As electrolytes, acetonitrile (MeCN) or dichloromethane in the presence of conducting salts such as tetrabutylammonium hexafluorophosphate (TBAPF₆) are well-established. It is recommended to use ferrocene/ferrocenium (Fc/Fc⁺) as external reference for each measurement to make electrochemical potentials comparable [31]. Detailed electrochemical characterization of P3HT films has been performed, for example, by Trznadel et al. [30] and Skompska et al. [32].

A typical reversible anodic oxidation cycle of a P3HT film is shown in Fig. 2b, in which the oxidation onset potential $E_{\text{onset}}^{\text{ox}}$ is marked. It is assumed that the onset potential values in cyclic voltammograms correspond to the oxidation/reduction of the polymer chains with the largest conjugated π -system. Because the oxidation corresponds to the removal of electrons from the highest occupied molecular orbital (HOMO), and the reduction to adding electrons to the lowest occupied molecular orbital (LUMO), the onset oxidation and reduction potentials are closely related to the HOMO and LUMO energies. From the graph in Fig. 2c, an $E_{\text{onset}}^{\text{ox}} = 0.02$ V (versus Fc/Fc⁺) and an $E_{\text{onset}}^{\text{red}} = -2.26$ V (versus Fc/Fc⁺) can be determined for a P3HT film with a weight-averaged molecular weight (M_w) of 112 kg/mol and a polydispersity index (PDI) of 2.4. The graph also contains data on the in-situ conductance behavior of the P3HT film, which was measured in an electrolyte-gated transistor configuration (for the method of CV with in-situ conductance measurements see, for example, [33]). One can see that only upon doping (oxidation or reduction) does the otherwise nonconducting P3HT film become conducting.

From the onset potential values of the oxidation and reduction, the HOMO and LUMO levels, respectively, of the polymer can be calculated according to the following equations [34]:

$$E(\text{HOMO}) = - (E_{\text{onset}}^{\text{ox}} (\text{vs. Fc/Fc}^+) + 5.1) [\text{eV}] \quad (1)$$

$$E(\text{LUMO}) = - (E_{\text{onset}}^{\text{red}} (\text{vs. Fc/Fc}^+) + 5.1) [\text{eV}] \quad (2)$$

For the P3HT film in Fig. 2c, this leads to a HOMO level of -5.12 eV and a LUMO level of -2.84 eV. In the literature, a factor of 4.8 eV instead of 5.1 eV is often used, which dates back to a 1995 publication by Pommerehne and coworkers [35]. For a discussion of the validity of the approach of using onset potentials for HOMO/LUMO determination we refer to [33, 34].

From the HOMO and LUMO level, Eq. (3) can be used to estimate the electrochemical band gap, which is a critical quantity for polymer-based organic photovoltaics:

$$\text{band gap} = |E(\text{HOMO}) - E(\text{LUMO})| \quad (3)$$

The electrochemical band gap should not be confused with the optical band gap, which is typically derived from the onset of absorption in thin film absorption spectra. Optical spectra give information about the optical excitation of an electron from the ground to the first excited state, whereas electrochemical oxidation/reduction produces real charged species, i.e., cations and anions. A combination of HOMO determination by electrochemistry and LUMO determination by subtracting the optical band gap is not recommended.

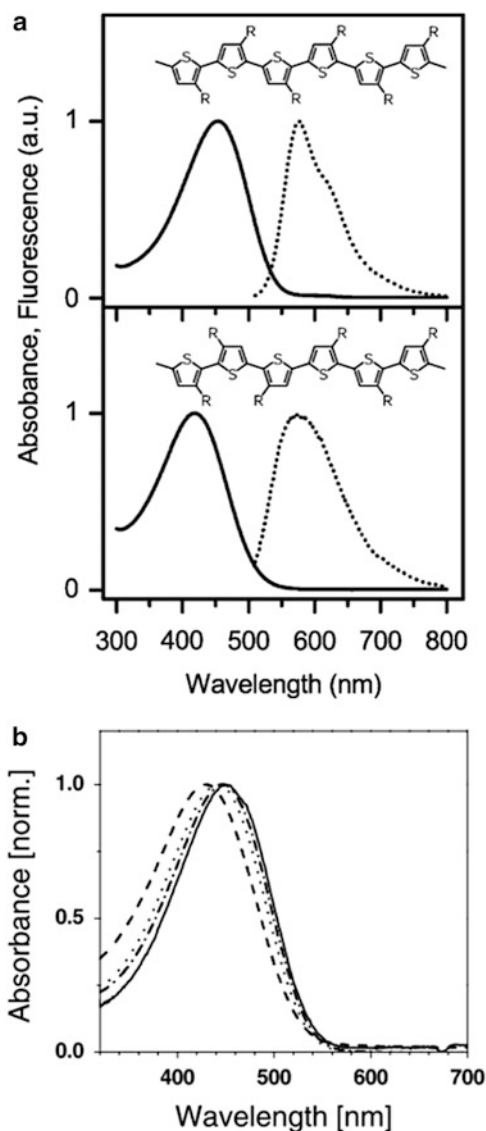
Scharber et al. have proposed a relation between the HOMO of the polymer and the open circuit voltage V_{oc} , which was used to estimate the maximum efficiency of bulk-heterojunction solar cells for a number of material combinations, including P3HT and phenyl-C61-butyric acid methyl ester (PCBM) [36]. As an alternative to energy level determination with electrochemistry, the method of photoelectron spectroscopy can be used: Kahn and coworkers used a combination of direct and inverse photoemission spectroscopy complemented by near edge X-ray absorption fine structure (NEXAFS) for determination of the HOMO and LUMO energy levels and the energy gap between the LUMO of the acceptor and the HOMO of the donor [37].

2.3 Optical Properties of P3HT Solutions

P3HT is soluble in a variety of solvents, which enables easy and cheap processability from solution. Optical spectroscopy in solution gives information about the conjugation of isolated molecules, usually in the absence of interchain packing effects. In solution, P3HT exhibits one broad absorption peak without structural features, which is associated with isolated chains in a coiled conformation [38]. Both repulsive interactions between successive monomer units and interactions between the solvent and the side chains drive a dihedral twist of the polymer backbone in solution [17]. Barbara and coworkers studied the impact of regioregularity on the conformation of a single chain by means of single-molecule fluorescence excitation polarization spectroscopy [39]. Thereby, they observed more ordered conformations for regioregular chains, whereas the incorporation of HH and TT couplings resulted in a wider distribution of conformations due to unfavorable side chain interactions. This is reflected in the absorbance and fluorescence spectra of P3HT solutions of different regioregularity (shown in Fig. 3a). In chloroform solution, regioregular P3HT shows absorption and fluorescence maxima at 454 and 577 nm, respectively, whereas the peak maxima are blue-shifted to 420 and 572 nm in the case of regiorandom P3HT. This blue shift has been reported by several groups [40–42] and reflects a decreased conjugation length, which stems from a sterically driven twist of the backbone. For regioregular P3HT, the conjugation length of a single chain is further affected by the chain length. Figure 3b

Fig. 3 (a) Absorbance (solid line) and fluorescence (dotted line) spectra of regioregular P3HT with 97% HT-HT coupling (top) and regiorandom P3HT with 64% HT-HT coupling (bottom) in chloroform solution [39]. (b)

Absorbance of regioregular P3HT in chloroform solution as a function of molecular weight. The fractions were obtained by successive solvent extraction in ethyl acetate (dashed line), hexane (dotted line), dichloromethane (dashed-dotted line), and chloroform (solid line) [17]. (Reprinted with permission from Adachi et al. [39]. Copyright (2011) American Chemical Society. And reprinted with permission from Zen et al. [17]. Copyright (2004) Wiley-VCH)



shows solution spectra of regioregular P3HT in chloroform for four fractions of different molecular weight achieved by successive extraction in ethyl acetate, hexane, dichloromethane, and chloroform. The number-average molecular weight (M_n) of these fractions was 2.2 kg/mol (PDI = 1.43), 5.6 kg/mol (PDI = 1.18), 13.8 kg/mol (PDI = 1.48), and 19.0 kg/mol (PDI = 1.35). For regioregular P3HT, increasing the molecular weight leads to a slight bathochromic shift of the absorption maximum in solution, which results from an increase in the average conjugation length along the polymer backbone [17, 30].

The use of poor solvents or solvent mixtures can further allow aggregation and crystallization directly from solution, which is the subject of the following section. This aggregation is accompanied by a bathochromic shift of the absorption maxima and the appearance of a vibronic fine structure (see also Sect. 3). In the extreme case of solid-state spectra of P3HT films, these effects are even more pronounced, with the spectra also becoming more structured for high molecular weights (see Sect. 4.1.1).

3 Crystallization from Solution

The rigidity and planar conformation of the conjugated backbone of many semi-conducting polymers such as regioregular P3HT allows efficient packing and crystallization. However, due to the difficulty of forming ordered crystalline structures from interpenetrating and entangled polymer chains of high rigidity, there are very few publications on single crystals of polymeric semiconductors [43]. Only recently has the growth of P3HT single crystals from solution using a self-seeding approach been reported [44]. The single crystalline nature of the deposited material and its identification as the form II polymorph was performed by Brinkmann via transmission electron microscopy coupled with electron diffraction (TEM/ED). For a more detailed crystal structure and polymorph discussion we refer to Sect. 4.1.2 and the article by Brinkmann et al. in this book [45].

Although insulating polymers such as PE crystallize in 2-dimensional (2D) lamellar sheets, conjugated polymers like P3HT typically form high aspect ratio, 1D nanocrystals (nanofibrils, nanowhiskers, nanofibers, and nanorods) [46]. Aggregation is driven by strong π - π interactions perpendicular to the conjugated backbone, as well as by hydrophobic interactions of the side chains.

In 1993, Ihn et al. were the first to report crystallization of P3HT nanocrystals from a dilute solution of a poor solvent [47]. Nanofibrils were grown from cyclohexanone (0.05%) by slow cooling of the solution from 50°C to room temperature (25°C/h). After deposition from solution on TEM grids, nanofibrils with a width of around 15 nm, a height of 5 nm, and a length of around 10 μ m were evidenced by TEM. Figure 4a shows the bright-field image and the corresponding electron diffraction pattern of P3HT nanofibrils grown from cyclohexanone. A representative AFM height image of similar nanofibrils is given in Fig. 4b. The precise packing of the chains within the nanofibrils was determined by electron diffraction and X-ray analysis and is schematically presented in Fig. 4c. The polymer backbone packs normal to the long axis of the fibril (i.e., the π -stacking is oriented along the fibril direction), whereas the alkyl chains point perpendicular to the substrate. This arrangement is also referred to as edge-on orientation (see also Sect. 4.1.2). Although the height of the fibrils relates to only two or three layers of P3HT chains, the fibril length of around 10 μ m demonstrates the strong packing tendency in the π -stacking direction. The fact that the (number) average contour length of the chains (around 65 nm), which was calculated on the basis of the (number) average

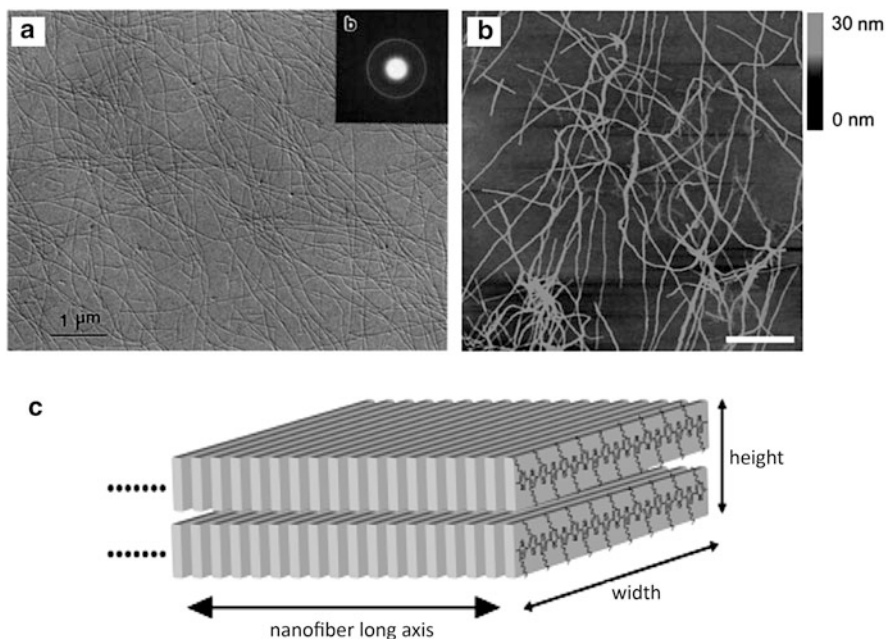


Fig. 4 (a) TEM image and the corresponding electron diffraction pattern (*inset*) of P3HT nanofibrils crystallized from cyclohexanone solution (0.05 wt%) [47]. (b) AFM height image of P3HT nanofibrils grown from a solution mixture of anisole and chloroform (4:1 vol%) and deposited on silicon wafers by spin-coating [48]. (c) Schematic representation showing the molecular orientation within a P3HT nanofibril [48]. (Reprinted with permission from Ihn et al. [47]. Copyright (1993) Wiley-VCH. And reprinted with permission from Samitsu et al. [48]. Copyright (2008) American Chemical Society)

molecular weight of 29 kg/mol, exceeds the width of the nanofibrils suggests that the chains fold back and forth in order to be incorporated into the nanostructures, a typical feature of semicrystalline polymers. Zhai and coworkers could further show that the fibril width increases with molecular weight, but saturates above a critical value of around 10 kg/mol (M_n) [49]. Below the critical molecular weight, nanofibrils are assumed to be formed by extended chains that span the width of the fibrils. Above the critical molecular weight, chain folding takes place and leads to a saturation of fibril width. The fold-length is dependent on the crystallization temperature in solution, which is characteristic of the crystallization of polymers.

Since the seminal work of Ihn et al. in 1993, a large number of publications have followed that deal with the structural and optical characterization of nanofibrils, but also address their performance in devices such as organic field-effect transistors (OFETs) and organic solar cells (OSCs) [47, 48, 50–53]. In general, two common approaches for P3AT nanofibril production are described in the literature [52]: (1) the whisker method and (2) the mixed solvent method. For both approaches, the growth of 1D nanocrystals is driven by strong π – π -interactions and unfavorable interactions between the solvent and polymer backbone under limited solubility.

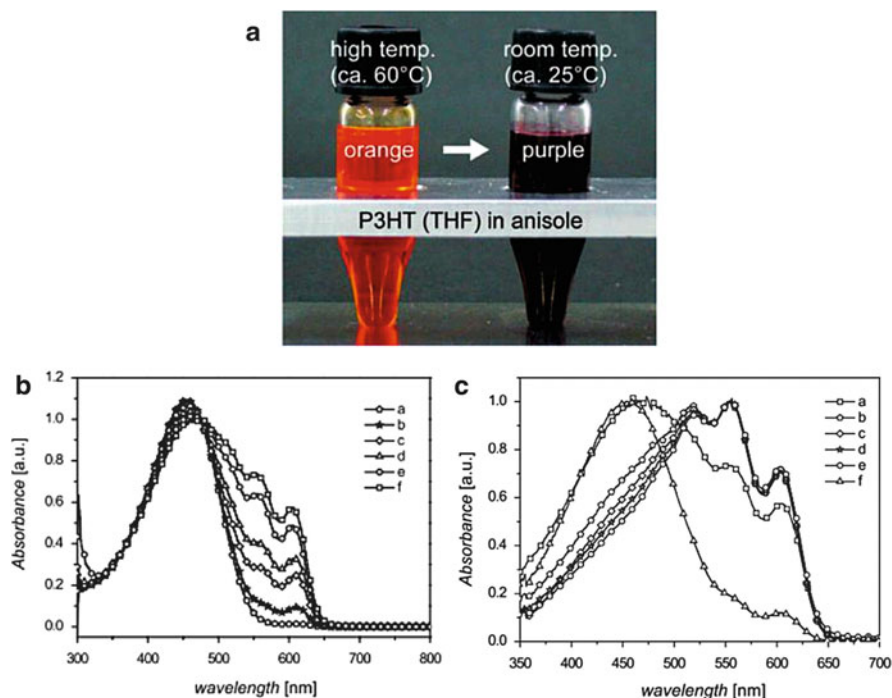


Fig. 5 (a) Photographic image of P3HT (Soxhlet-extracted from THF) in anisole (0.05 wt%) at 60°C (*left*) and room temperature (*right*) [48]. (b) Absorption spectra of P3HT in *p*-xylene (1 wt%) after dissolution at 80°C and subsequent cooling to room temperature at 20°C/h. Evolution of the solution was followed at room temperature, with the spectra being taken after (a) 2 h, (b) 4 h, (c) 6 h, (d) 21 h, (e) 28 h, and (f) 48 h [50]. (c) Absorption spectra of P3HT in *p*-xylene (1 wt%) (a) before centrifugation and filtration, (b) after the first centrifugation step, (c) after two centrifugation steps, (d) after five centrifugation steps, (e) after two centrifugation and one filtration steps, and (f) absorption spectrum of the collective filtrates [50]. (Reprinted with permission from Samitsu et al. [48]. Copyright (2008) American Chemical Society. And reprinted with permission from Berson et al. [50]. Copyright (2007) Wiley-VCH)

Using the whisker method introduced by Ihn et al. [47], Guillerez and coworkers followed the formation of P3HT nanofibrils in solution, prepared using a marginal solvent, by optical spectroscopy [50]. Aggregation in solution is accompanied by a drastic color transition from orange to purple/violet (see Fig. 5a), denoting a significant change in the physical conformation of the polymer chains, as reported by Ihn et al. and Samitsu et al. [47, 48]. This makes in-situ linear absorption spectroscopy an elegant and simple tool for monitoring aggregate formation in solution. Guillerez et al. reported crystal growth in *p*-xylene, which is a poor solvent for P3HT at room temperature, whereas complete dissolution of the polymer chains occurs at elevated temperature and gives rise to a single, broad absorption peak. The evolution of the solution spectrum after cooling to room temperature at a controlled rate is illustrated in Fig. 5b. After cooling, additional vibronic structures at

525, 555, and 610 nm gradually emerge, which is indicative of the formation of highly ordered structures. The appearance of an isosbestic point at 475 nm clearly suggests the presence of two different states in the polymer solution. This is explained by a transition of completely dissolved polymer chains into aggregated stacks without intermediate states.

A combination of centrifugation and filtration was used to isolate the fibers in the form of a crystalline powder that forms stable suspensions in *p*-xylene (1 wt%). The filtrate mainly comprised well-dissolved polymer chains, as can be seen from Fig. 5c. Size-exclusion chromatography further demonstrated that the nanofibrils were mainly composed of high molecular weight chains ($M_w \approx 46$ kg/mol, PDI = 2.3), whereas shorter chains remain dissolved in solution ($M_w \approx 38$ kg/mol, PDI = 2.8).

The mixed-solvent method is based on use of a combination of good and poor solvents [52, 54–56]. Thereby, unfavorable interactions between the polymer and the poor solvent drive the aggregation of chains into nanostructures. Kiriy et al. showed that highly aggregated 1D nanostructures of P3HT with a helical conformation of the backbone can be obtained by adding hexane to a solution of P3HT in CHCl_3 . Hexane acts as a selective solvent for the side chains, but is a rather poor solvent for the conjugated backbone and, hence, favors π – π -interactions and aggregation [54]. In contrast, Sun et al. started with a solution of P3HT in a marginal solvent and demonstrated that, by adding small amounts of a good solvent, the crystallinity of nanofibrils could be improved as a result of an increased flexibility and organization of the chains within the aggregates [52]. Self-assembly can further be triggered by ultrasonication of the solvent mixture, as reported by Kim and coworkers [57].

Zhai and coworkers showed that P3HT nanofibrils can grow into highly ordered 2D nanoribbons, whose structure is shown in Fig. 6 [49]. However, this requires a well-defined nanofibril surface, which is present only in P3HT of low molecular weight for which chain folding is unlikely. Nanofibril growth was achieved by cooling a solution of P3HT in a marginal solvent from 90°C to room temperature. For $M_n > 10$ kg/mol, anisole (0.05 mg/mL) was used as a marginal solvent, whereas crystallization of low molecular weight P3HT ($M_n < 10$ kg/mol) required the use of a co-solvent of poor dissolving power (anisole/dimethylformamide (DMF), 1:2 vol%, 0.2 mg/mL) to reduce the solubility of the short chains. At first, crystallization from solution results in the formation of 1D nanofibrils, which then act as nucleating points for further growth along the [100] direction via alkyl chain interactions. For high molecular weight P3HT with M_n above a critical value of 10 kg/mol, chain folding results in nanofibrils with more defects, which prevents further growth of the nanofibrils into 2D nanoribbons.

A serious consequence of polymer crystallization in solution is gel formation, which is a severe issue regarding, for example, inkjet printing of polymeric semiconductors because gelation dramatically shortens the lifetime of electronic inks. The gelation mechanism has been intensively studied by Nandi and coworkers, who describe the gel formation of P3HT as a two-step process [58, 59]. In phase I, single isolated chains undergo a coil-to-rod transformation, and phase II involves the

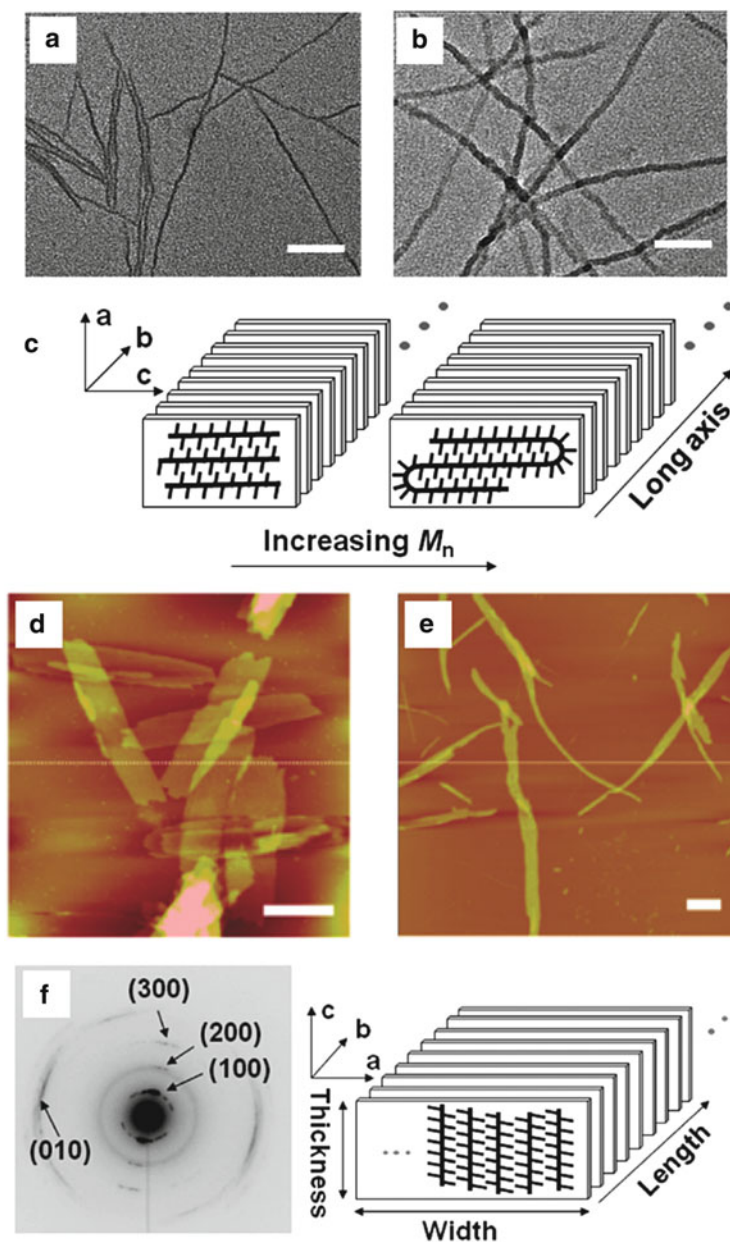


Fig. 6 (a, b) TEM images of P3HT fibrils grown from solution by the whisker method at 25°C: (a) $M_n = 6.0$ kg/mol, 0.2 mg/mL in DMF/anisole (2:1 vol%) and (b) $M_n = 15.6$ kg/mol 0.05 mg/mL in anisole [49]; scale bars: 100 nm. (c) Extended and folded polymer chains within the nanofibrils for $M_n < 10$ kg/mol and $M_n > 10$ kg/mol, respectively. (d, e) AFM phase images of P3HT nanoribbons prepared by the whisker method at 25°C and deposited on silicon wafers by spin-coating of (d)

crystallization of rods into fibrillar structures. Koppe et al. further assume that, after aggregation, ordered domains link to each other and form a gel, which results in an increase in viscosity (see Fig. 7) [51]. Aggregation and gelation occur most intensely and quickly for high molecular weight chains and can be delayed or even suppressed by “dilutants” such as PCBM and P3HT chains of low molecular weight. Furthermore, side chain length and regioregularity play a crucial role in the gelation process [58, 59].

For all the approaches described so far, crystal formation takes place in solution before the deposition of the polymer on a substrate. The deposition of pre-aggregated nanocrystals is typically achieved by means of drop-casting, spin-coating, or dip-coating. The performance of nanofibril-based films of polythiophenes has been intensely investigated in devices such as OFETs and OSCs [50, 52, 55, 57, 60–66]. Merlo and Frisbie reported hole mobilities of up to $0.06 \text{ cm}^2/\text{V s}$ for single P3HT nanofibrils, demonstrating the high degree of order within the fibrils [60, 61]. Samitsu et al. further showed for P3AT of different side chain lengths that charge carrier transport in single fibrils is much more effective than between fibrils in a network, suggesting a transport barrier between adjacent fibrils (see Fig. 8) [63]. In contrast to thin films of P3AT cast from solutions prepared using a good solvent, nanofibril-based films exhibit hole mobilities that are relatively independent of the side chain length, which results from the high in-plane order of the chains within the fibrils (edge-on), whereas the molecular orientation in cast films is strongly affected by the alkyl chain length during solution-casting [53]. In bulk-heterojunction solar cells, P3HT nanofibrils yield high power conversion efficiencies of 3.9% [55] in combination with PCBM.

4 Thin Film Properties

Highly crystalline layers of P3HT can be obtained by pre-aggregation of nanofibrils in solution followed by deposition of the aggregated nanostructures on a substrate, which allows decoupling of crystallization from the film deposition process. However, device fabrication requires cheap and fast techniques to generate homogeneous films on a large scale. Consequently, controlled crystal formation in solution is difficult to implement for device fabrication. Deposition of conjugated polymers is typically pursued from solutions prepared using a good solvent like chloroform via various techniques such as spin-coating, doctor-blading, dip-coating, and inkjet-printing. In these fast processes, crystal formation takes place during drying of the

Fig. 6 (continued) $M_n = 6.0 \text{ kg/mol}$, 0.2 mg/mL in DMF/anisole (2:1 vol%) and (e) $M_n = 10.2 \text{ kg/mol}$, 0.05 mg/mL in anisole; scale bars: 500 nm. (f) Selected area electron diffraction of P3HT nanoribbons (10.2 kg/mol) corresponding to (e). Molecular arrangement within P3HT nanoribbons is shown on the right. (Reprinted with permission from Liu et al. [49]. Copyright (2009) American Chemical Society)

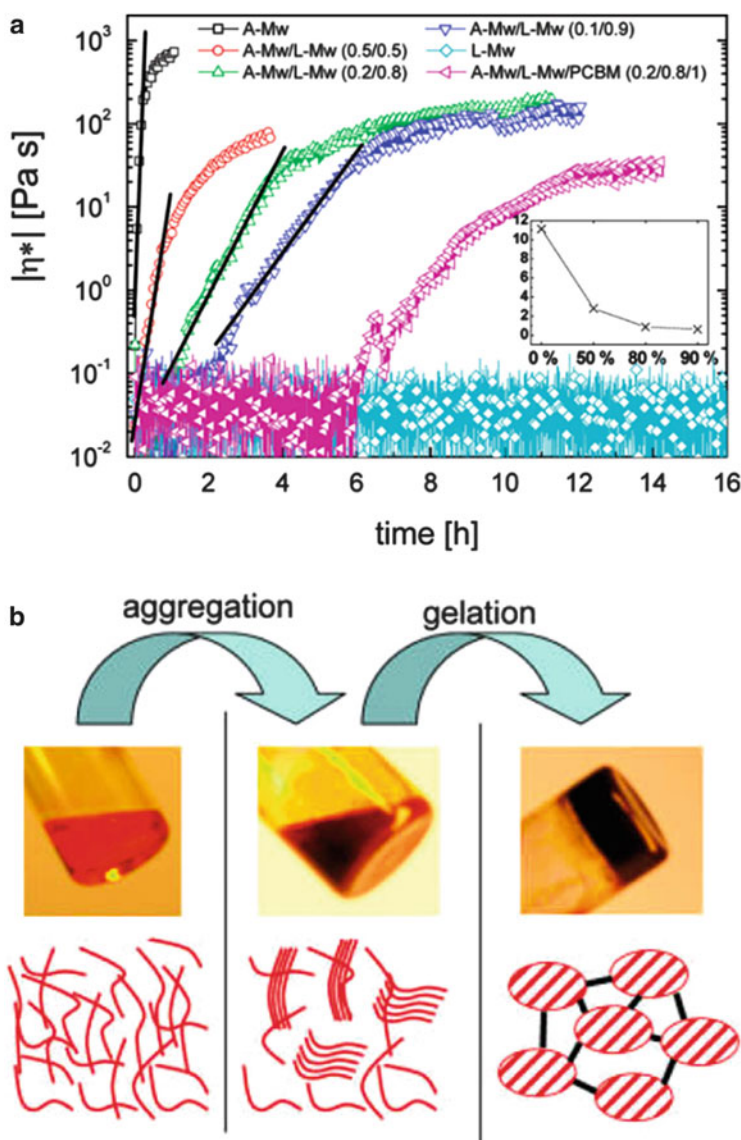


Fig. 7 (a) Rotational rheometer viscosity measurements of P3HT solutions in *o*-xylene (1 wt%) at 25°C for different molecular weight compositions obtained by mixing A- M_w ($M_w = 72.8$ kg/mol) and L- M_w ($M_w = 26.2$ kg/mol) in different proportions [51]. Full lines were generated by linear fits to the experimental viscosity evolution. Inset: the slope of the linear fits for increasing contents of L- M_w mixed with A- M_w (0, 50, 80, and 90 wt%). (b) Photographic images and sketches of the two-step process of polymer gelation for P3HT ($M_w = 72.8$ kg/mol) in *o*-xylene solution (1 wt%). (Reprinted with permission from Koppe et al. [51]. Copyright (2009) American Chemical Society)

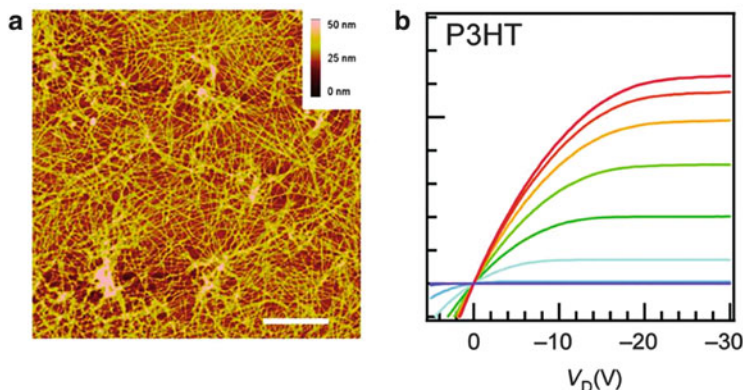


Fig. 8 A network of P3HT nanofibrils was grown from a solvent mixture of anisole and chloroform (4:1 vol%, 0.05 wt%) by slowly cooling the solution from 70°C to 20°C (25°C/h) [63]. The fibrils were deposited on transistor substrates by spin-coating. (a) AFM height image; scale bar: 1 μm . (b) Output characteristics of a nanofibril-based bottom gate, bottom contact transistor with V_G ranging from +5 V to -30 V (-5 V/step). (Reprinted with permission from Samitsu et al. [63]. Copyright (2010) American Chemical Society.)

film and therefore usually under nonequilibrium conditions. The microcrystalline morphology is strongly dependent on the film processing conditions, including the coating technique itself, but also on the choice of solvent and the nature of the substrate [5, 67–72]. In addition to the precise deposition conditions, the molecular parameters of the polymer (molecular weight and regioregularity) have a strong impact on the morphology [17, 18, 73–75].

In the following section, we review the influence of these different parameters on the thin film morphology, and also their impact on the functional properties in devices. The impact of thin film morphology on both the optical and electrical properties is discussed. The section is structured as follows: First, visual inspection of P3HT thin films is described, with absorption spectroscopy being an excellent tool for understanding intra- and interchain order in thin films. Then, the influence of molecular parameters and processing conditions on the mesoscopic and microcrystalline morphology is discussed. Some findings on the influence of morphology on charge transport are also included.

4.1 Preparation and Characterization of P3HT Films

4.1.1 Optical Properties of Thin Films

When P3HT films are deposited from solutions prepared using good solvents, significant color changes can be detected that range from orange to purple depending on the regioregularity and the molecular weight of the batch. Thin film

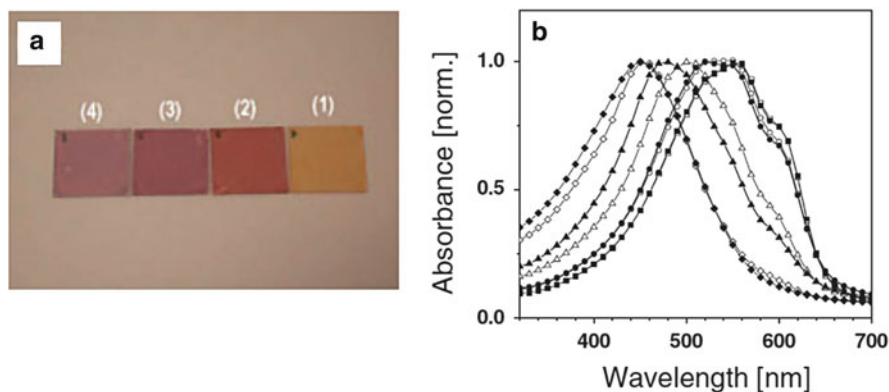


Fig. 9 Optical properties of P3HT thin films as a function of the molecular weight [17]: (a) Optical photographs of P3HT layers spin-cast from the ethyl acetate (1), hexane (2), dichloromethane (3), and chloroform (4) fractions. (b) Absorption spectra of P3HT thin films of the ethyl acetate (*open diamond, filled diamond*), hexane (*open triangle, filled triangle*), dichloromethane (*open circle, filled circle*), and chloroform (*open square, filled square*) fractions. *Open and filled symbols* correspond to as-cast and thermally annealed layers (5 min. at 150°C), respectively. (Reprinted with permission from Zen et al. [17]. Copyright (2004) Wiley-VCH)

spectra of regiorregular P3HT resemble the solution spectra of regioregular P3HT (shown in Fig. 3), consisting of a broad and almost featureless absorption band [76]. This observation is related to the fact that regiorregular P3HT forms mainly amorphous layers due to the weak tendency for intermolecular packing, which is impeded by the sterically driven twist of the backbone. Therefore, the physical conformation of the chains is similar to that of regioregular P3HT in the solution state. By contrast, film spectra of regioregular P3HT are significantly red-shifted and exhibit well-defined vibronic features in the low-energy part of the spectrum, which is attributed to the presence of π -stacked aggregates in which chain twisting is strongly constrained, leading to flat molecules with extended conjugation [76]. Additionally, the optical properties are strongly dependent on the molecular weight. This is illustrated in Fig. 9, which shows both photographs and absorption spectra of P3HT thin films of different molecular weight after solution-casting and thermal annealing, respectively [17]. The fact that the thin film spectrum of low molecular weight P3HT resembles the solution spectrum indicates that a large number of the chains adopt a twisted conformation in the solid state. Studies on thermochromism strengthen the interpretation that the variation in optical absorption is connected to the conformation of the polymer chain [17]. Heating a thin P3HT film of intermediate molecular weight (hexane fraction, $M_n = 5.6$ kg/mol) to 210°C leads to a strong color change from red to yellow/orange, most probably due to a twisting of the backbone. By contrast, little and almost no change is observed for high ($M_n = 19$ kg/mol) and low ($M_n = 2.2$ kg/mol) molecular weight P3HT, respectively.

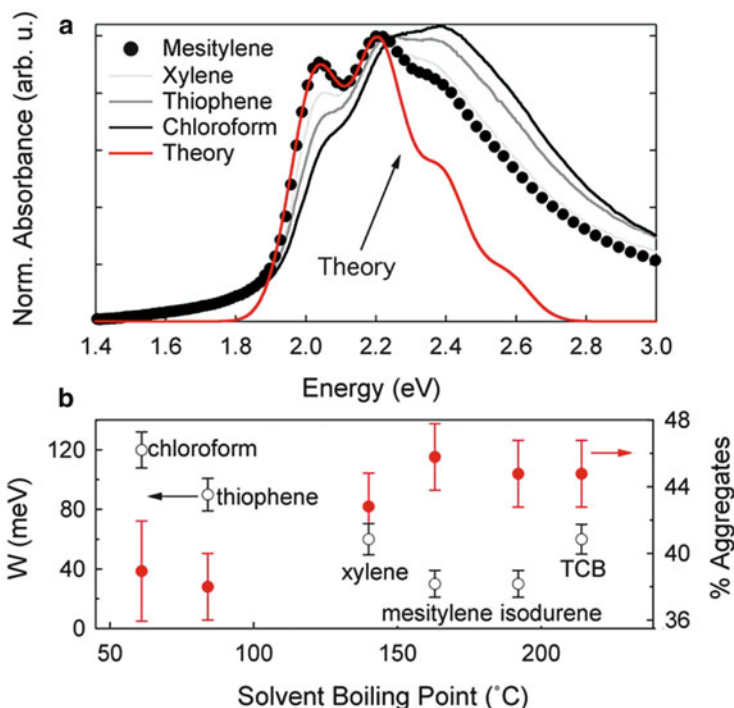


Fig. 10 (a) Normalized absorption spectra of P3HT films spin-coated from various solvents. A theoretical spectrum for mesitylene is depicted in red [78]. (b) Exciton bandwidth (W) (left axis, open black symbols) and percentage of film that is formed of crystalline aggregates (right axis, red symbols) as a function of the casting solvent. (Reprinted with permission from Clark et al. [78]. Copyright (2009) American Institute of Physics)

Absorption spectroscopy is a good tool for determination of the degree of intra- and interchain order within P3HT thin films. A detailed and quantitative analysis of the absorption spectrum of regioregular P3HT was proposed by Spano and coworkers [6, 77, 78]. For a thin P3HT film, two parts of the absorption spectrum can be distinguished, as shown in Fig. 10a. The high energy part of the spectrum is attributed to disordered chains forming intrachain states, most probably related to chains in the amorphous part of the film, whereas the lower energy part denotes weakly interacting H-aggregates in crystalline regions of the layer. Two peaks can be identified in the lower energy part: A_{0-0} transition at 620 nm (2.0 eV) and A_{0-1} transition at 570 nm (2.2 eV). The free exciton bandwidth (W) within the crystalline domains is associated with the intensity ratio of the A_{0-0} and A_{0-1} peaks by the following equation:

$$\frac{A_{0-0}}{A_{0-1}} = \left(\frac{1 - 0.24W/E_p}{1 + 0.073W/E_p} \right)^2 \quad (4)$$

where E_p describes the energy of the main intramolecular vibration coupled to the electronic transition.

The Spano model provides an easy approach for estimating the aggregate content and intrachain order in P3HT thin films by simply exploiting the absorption spectrum, as shown in Fig. 10b. The model can be further used to follow crystallization of P3HT from solution, distinguishing between well-dissolved chains and chains incorporated in crystalline nanocrystals (compare with Sect. 3).

4.1.2 Mesoscale Morphology

Molecular Parameters

It is well established in the literature that the morphology of regioregular P3HT is highly affected by molecular parameters of the polymer such as molecular weight, regioregularity, and polydispersity [16–18, 73–75, 79–81]. In 2003, Fréchet and coworkers showed a clear correlation of the crystalline morphology and the molecular weight of poly(3-alkylthiophene)s, which is also accompanied by dramatic changes of the field-effect mobility [73].

Low molecular weight P3HT of $M_n < 10$ kg/mol forms well-defined nanorods whose widths show a linear increase with molecular weight and correspond well to the contour length of the chains (Fig. 11a) [75, 79]. This suggests that the nanorods are composed of extended chains, with the backbone being in the plane of the film and oriented perpendicular to the long axis of the nanorod. This structure is supported by X-ray diffraction (edge-on orientation; see end of this section). For higher molecular weights of $M_n > 10$ kg/mol, the periodicity of the nanofibrils saturates and less-defined, nodule-like morphologies appear (see Fig. 11b). Here, the contour length of the chains is much higher than the width of the nanofibrils. The linear increase in nanocrystal width with increasing molecular weight, followed by saturation (see Fig. 12), is attributed to chain folding [79].

Bending of P3AT chains in thin films was visualized by Mena-Osteritz and Grévin et al. after self-organization on highly oriented pyrolytic graphite (HOPG) via scanning tunneling microscopy [82, 83]. As a result of the relatively high stiffness of the conjugated backbone, chain folding is believed to induce stress on the stacking of the chains, which gives rise to decreased order and less-defined nanostructures in high molecular weight P3HT.

Regarding charge transport, by increasing the molecular weight M_n over one order of magnitude from around 4–36.5 kg/mol, the charge carrier mobility is observed to increase over almost four orders of magnitude, improving from 10^{-6} to 10^{-2} cm²/V s [73]. Zen et al. propose that the field-effect mobility is highly affected by the crystallinity of the sample [17, 74]. Despite the high perfection of

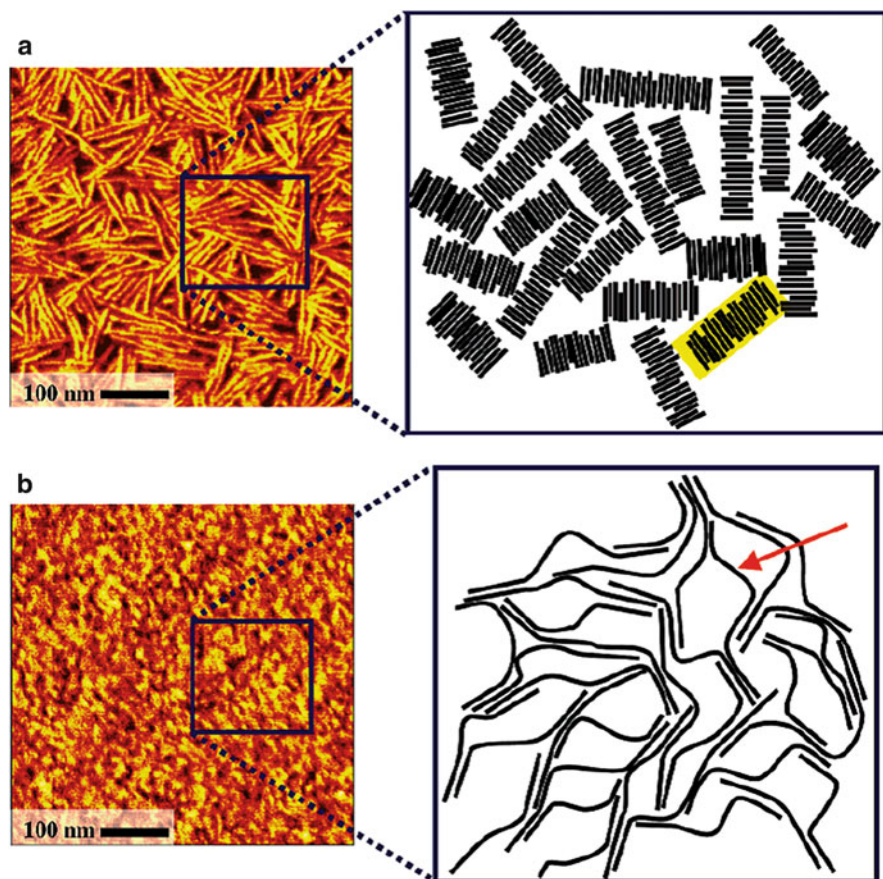


Fig. 11 Morphology of P3HT films directly after spin-coating: (a) Ribbons of a low molecular weight sample ($M_n < 4$ kg/mol) in an extended chain configuration [18]. (b) Less-defined morphology of a high molecular weight sample ($M_n > 30$ kg/mol) with tie molecules (marked by a red arrow) bridging crystalline domains. (Reprinted with permission from Kline et al. [18]. Copyright (2005) American Chemical Society)

the crystalline nanorods in low molecular weight P3HT, charge transport seems to be mainly determined by twisted chains in the amorphous matrix. In contrast, chains of high molecular weight adopt a planar chain conformation, enabling strong π - π -interactions and hence efficient charge transport. Kline et al. take into account that charges become trapped at grain boundaries between nanocrystals [18, 73]. In low molecular weight P3HT, the nanorods are poorly interconnected (as evidenced by AFM), which results in severe charge trapping. Longer chains can bridge the amorphous zones between the crystallites and soften the boundaries, leading to improved macroscopic charge transport. The presence of such interconnecting chains in high molecular weight P3HT, also referred to as tie-chains, is illustrated in Figs. 11 and 13. In general, the morphology of high molecular weight P3HT is

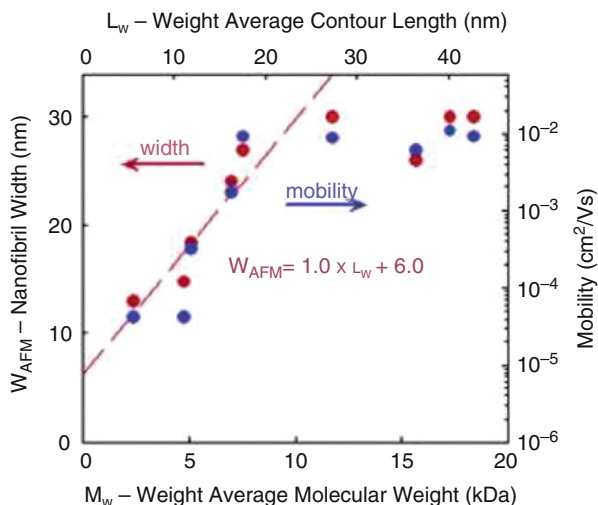


Fig. 12 Evolution of P3HT nanofibril width W_{AFM} and hole mobility μ as function of weight-average molecular weight M_w and weight-average contour length L_w [79]. Thin films were prepared by drop-casting from toluene (1 mg/mL). (Reprinted with permission from Zhang et al. [79]. Copyright (2006) American Chemical Society)

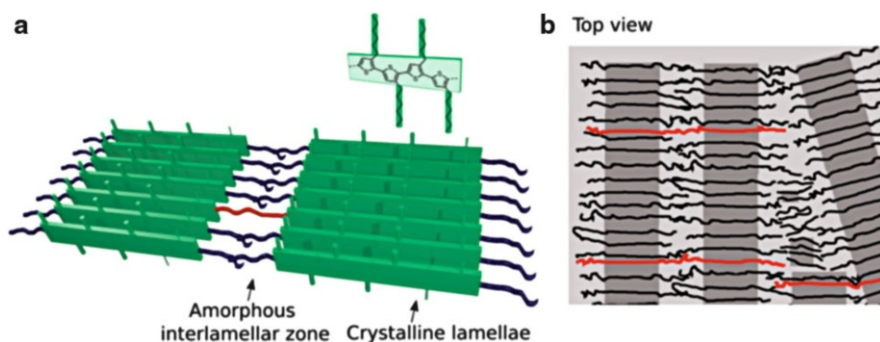


Fig. 13 Microstructure in P3HT thin films: (a) molecular arrangements of the polymer chains within the nanocrystalline lamellae, which are separated by amorphous domains; and (b) meso-scale morphology of P3HT consisting of crystalline lamellae (dark grey) separated by amorphous domains (light grey). Tie-chains connecting adjacent lamellae are shown in red. Image courtesy of Florian Fischer

composed of a mixture of ordered and amorphous regions. Crystalline lamellae formed of planar, stacked chain segments are separated by interlamellar amorphous domains comprising chain ends, chain folds, and long tie-chains, the latter interconnecting neighboring crystallites. Although little is known about the precise nature of these interconnections, qualitative considerations were proposed by

Salleo and coworkers in a recent publication [84]. On large length scales, polymer chains are flexible, whereas the backbone is rather rigid at the length scale of the persistence length. Therefore, the authors propose a weak bending of the polymer chains if the distance between adjacent crystallites is in the region of a few persistence lengths. These tie-chains with extended conjugation serve as an efficient charge transport pathway through disordered domains in high molecular weight P3HT.

Processing Conditions

Not only molecular parameters, but also the processing conditions strongly affect the thin film morphology. The literature on different deposition protocols and post-processing protocols is huge. In this section, we highlight some representative examples.

Typical solution deposition techniques are dip-coating, drop casting, and spin-coating, with the evaporation rate of the solvent increasing in the given order. The nanostructured morphology is most distinctive in the case of a slow drying of the film, when the polymer chains have sufficient time to self-assemble into nanocrystalline structures. Changes in the thin film morphology as a function of the solvent evaporation rate are illustrated in Fig. 14, which shows AFM images of P3HT films of four different molecular weights cast by three different methods under identical conditions. Dip-coating and spin-coating were performed from chloroform solution, whereas drop-cast films were obtained from a solvent mixture of chloroform and tetrahydrofuran (14:3, v/v). Fast solvent evaporation during spin-coating leads to rod-like structures only for low molecular weight samples, whereas layers of $M_n > 10$ kg/mol remain almost featureless. By contrast, slow solvent evaporation achieved by dip-coating results in well-defined nanostructures that are independent of the molecular weight. During the slow film drying process, the polymer chains can stack into ordered nanofibrils, even in the case of long chains. The impact of such a slow solvent evaporation achieved by dip-coating was further demonstrated by Heeger and coworkers, who studied charge transport in ultrathin dip-coated films with a thickness of a few nanometers [70]. The latter exhibit highly ordered structures, as evidenced by well-resolved bands in the optical absorption spectrum, which correlates with high mobilities reaching $0.2 \text{ cm}^2/\text{V s}$ in accumulation mode.

In spin-coated layers, the microcrystalline order is typically low, especially when low boiling point solvents such as chloroform are used. Order can be significantly improved by using high boiling point solvents such as trichlorobenzene (TCB), as evidenced by X-ray diffraction and AFM [69]. This also causes a significant enhancement of the charge carrier mobility to $0.12 \text{ cm}^2/\text{V s}$, which is around one order of magnitude higher than for layers cast from chloroform. Another approach to slow solidification was demonstrated by Cho and coworkers, who reported the formation of highly ordered 1D nanofibrils via spin-coating in a solvent vapor atmosphere [85]. Spin-coating was carried out from chloroform, and the amount of chloroform within the spin-coating chamber determined the solvent

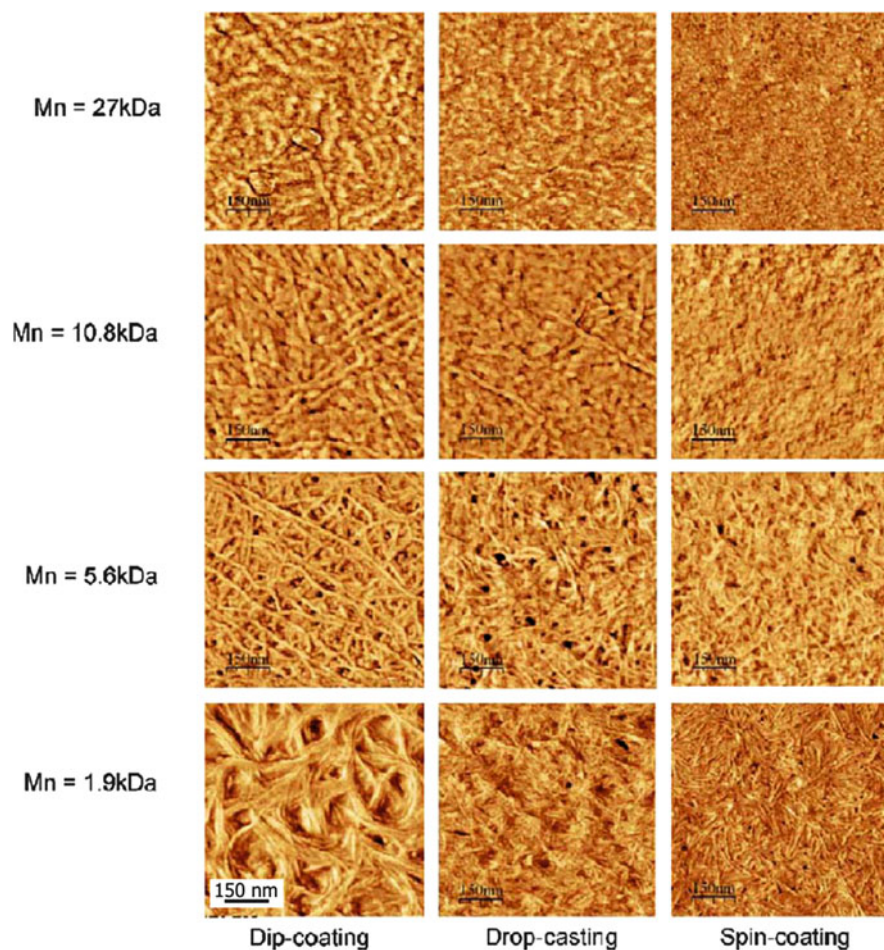


Fig. 14 AFM phase images of thin P3HT films of different molecular weight achieved by three different casting techniques [75]. (Reprinted from Verilhac et al. [75], Copyright (2006), with permission from Elsevier)

vapor pressure. Control of the solvent vapor pressure during solidification of the polymer enabled adjustment of the length of the resulting nanofibrils.

In 1996, Bao and coworkers compared the charge transport properties of P3HT layers deposited by spin-coating and drop-casting from different solvents [5]. Drop-cast films generally showed better charge transport, which was attributed to a higher degree of order achieved by the slow growth process of the film. However, the use of different solvents resulted in a significant scattering, and no clear evolution of the hole mobility as a function of the film drying time was found, which was related to differences in film quality. In order to achieve a better understanding of this behavior, a detailed structural investigation of drop-cast and spin-coated layers

from different solvents was accomplished in later years by Bao and coworkers [67, 68]. The fact that no clear correlation between the drying time and the field effect mobility could be found for drop-cast layers was attributed to the precise mesoscale morphology induced by different solvents, i.e., crystallinity, grain boundaries, branching of fibrils, and the degree of in-plane stacking. For further correlations between the charge carrier mobility and the processing conditions we refer to a recent review by Wuest and coworkers [86] and the article by Zaumseil in this book [87].

To summarize, the crucial parameters that affect hole mobility include: (1) the mesoscale morphology comprising the interconnectivity of crystalline domains and the presence of grain boundaries and (2) the $\langle 100 \rangle$ orientation distribution with respect to the substrate and, hence, the degree of in-plane π -stacking [67]. In the following section, studies on the orientation of the polymer chains with respect to the substrate are reviewed.

Texture and Orientation of Polymer Chains on Substrates

Before focusing on the texture of P3HT on substrates, research on structural models and the polymorphism into form I and form II is briefly mentioned.

From a crystallographic point of view, the a -axis corresponds to the (100) direction pointing in the direction of the alkyl chains, the b -axis (010) is the π - π -stacking direction, and the c -axis (001) corresponds to the direction along the polymer chain. Structural studies on P3ATs were initiated by Prosa in 1992, who also reported the presence of polymorphism into form I and II (see Fig. 15) [88, 89].

Prosa et al. initially reported an orthorhombic unit cell for form I [89]. In a later study, Tashiro et al. proposed other possible structures that are consistent with both experimental and simulated diffraction patterns [90]. Using electron diffraction, Brinkmann and Rannou found a monoclinic unit cell for form I P3HT [91]. This structure was challenged by Dudenko et al. [92]. Although it has not been possible to grow single crystals in form I (which makes the structure determination difficult),

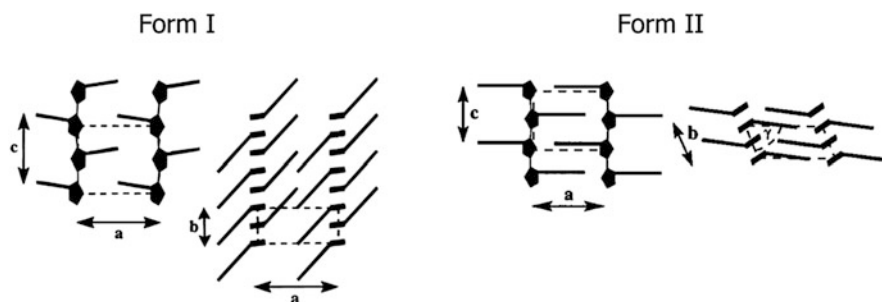


Fig. 15 Crystal structure of P3HT in form I and form II [88]. (Reprinted with permission from Prosa et al. [88]. Copyright (1996) American Chemical Society)

single crystals in form II were recently grown by a self-seeding approach from solution [44]. For a more in-depth discussion of the crystal structures we refer to [93] and Ref. [45] in this book.

Values of the degree of crystallinity are not usually discussed in the literature. This is because it is very difficult to determine the reference melting enthalpy ΔH_m of an ideal crystal of P3HT. A first value of 99 J/g was given by Malik and Nandi [94]. Only recently have optimized values of around 37 J/g been determined by DSC measurements and ^{13}C solid-state NMR measurements by Saalwächter and Thurn-Albrecht [16, 81], and values of around 50 J/g were found by Snyder and coworkers [95, 96]. Density measurements and correlations of the obtained densities to these melting enthalpies strongly suggest that values between 37 and 50 J/g seem to be correct [96].

Upon deposition from solution, two textures are mainly reported for P3HT thin films: edge-on and face-on. For an edge-on texture, the π -stacking is in the plane of the film, while the side chains point along the substrate normal (Fig. 16a). For a face-on texture, the polymer chains lie flat on the substrate with the π -stacking oriented along the substrate normal (Fig. 16b). In the literature, little is reported

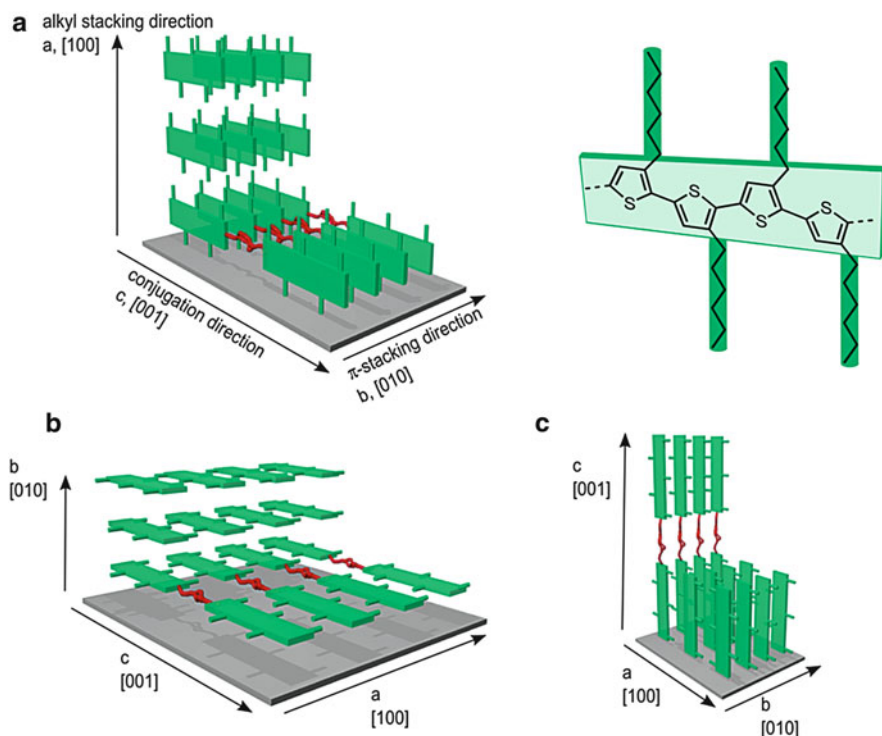


Fig. 16 Molecular orientation of P3HT in thin layers, with fast charge transport expected parallel to the chain axis and in the π -stacking direction, while the side chains act as barriers: (a) edge-on orientation, (b) face-on orientation, and (c) standing chains. Image courtesy of Florian Fischer

about standing chains of P3HT, where the polymer backbone stands vertically on the substrate (Fig. 16c) [97, 98]. The description of texture is not consistent in the literature, with some groups referring to the orientation of the chains and others denoting the orientation of crystalline grains with respect to the substrate. In this chapter, we refer to the molecular orientation of the polymer chains.

In general, the thermodynamically favored texture is assumed to be formed by edge-on oriented chains [1, 5, 68, 69]. This structure is obtained under conditions close to the equilibrium realized for slow casting methods such as drop-casting [1, 67, 68] and dip-coating, and by spin-coating from high boiling point solvents [69]. The face-on orientation is regarded as a kinetically trapped morphology, which is obtained by rapid drying of the layer [71]. This texture seems to be further favored for P3HT of low regioregularity [1] and for layers prepared under shear force, for instance via the friction transfer method [99] or mechanical rubbing [100] (see Sect. 4.2.1).

It is generally believed that fast charge transport occurs along the chain axis (*c*-axis) and in the π -stacking direction (*b*-axis), whereas the insulating side chains (*a*-axis) lead to charge barriers and low mobilities. Therefore, an edge-on orientation is highly desirable for OFETs since here high in-plane charge transport between the source and drain electrode is essential. The importance of molecular orientation for charge transport was first demonstrated by Sirringhaus and coworkers, who studied transistor properties for different textures [1]. In edge-on orientation, the field-effect mobility is more than 100 times higher than for chains in face-on orientation, which is attributed to the excellent charge transport along the chain axis and in the π -stacking direction.

The impact of the solvent evaporation rate on the texture was demonstrated by Bao and coworkers, who prepared P3HT layers from chloroform solution using two different methods, namely spin-coating and drop-casting (Fig. 17) [68]. In the slow drop-casting process, polymer chains have sufficient time to self-assemble into well-defined nanofibrils that are visible in AFM. In accordance with the morphology, the polymer chains adopt an edge-on orientation, as evidenced by grazing incidence X-ray diffraction (GIXRD) measurements. In stark contrast, AFM measurements of spin-cast layers show an almost featureless microstructure, while GIXRD reveals a predominant face-on texture.

DeLongchamp et al. studied the microstructure of P3HT spin-cast from chloroform for different spin speeds and found a remarkable change in the texture, which is shown in Fig. 18 [71]. With decreasing spin speed, a transition from mainly face-on to edge-on was observed. A reduction in spinning speed led to a slower evaporation of the solvent [101]. Therefore, this observation is in agreement with various reports in the literature showing that slow evaporation typically results in a higher degree of edge-on orientation [5, 70, 80, 102].

Besides the deposition conditions, the nature of the substrate can have a significant influence on the texture. Substrate treatment with self-assembled monolayers (SAMs) such as octadecyltrichlorosilane, hexamethyldisilazane, and γ -aminopropyltriethoxysilane results in an edge-on texture [72, 103–105]. By contrast, Chow and coworkers reported the formation of a face-on oriented P3HT

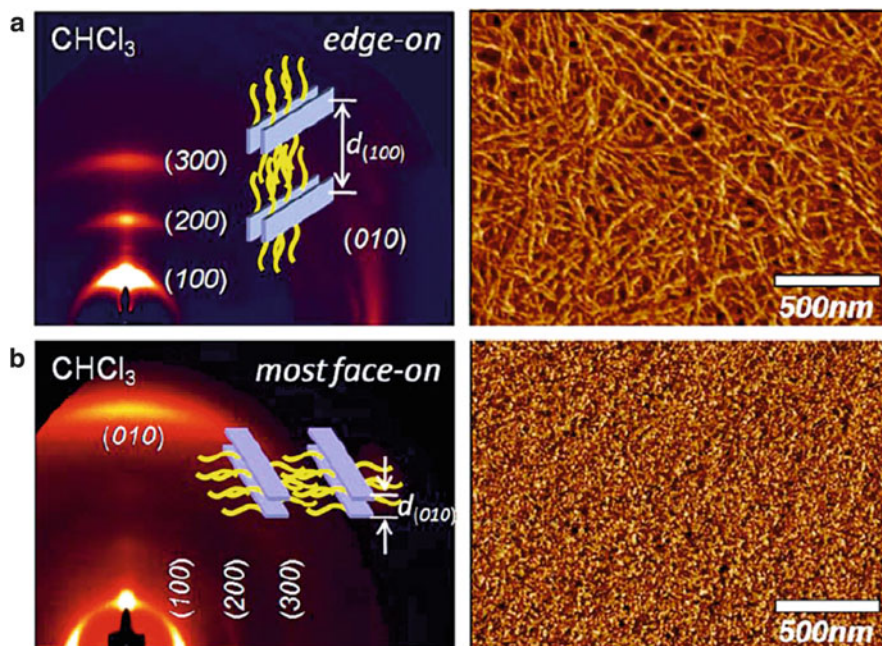


Fig. 17 Impact of processing conditions on the texture of P3HT [68]. GIXRD (*left*) and AFM measurements (*right*) of P3HT layers deposited from chloroform solution by (a) drop-casting and (b) spin-coating. (Reprinted with permission from Yang et al. [68]. Copyright (2007) American Institute of Physics)

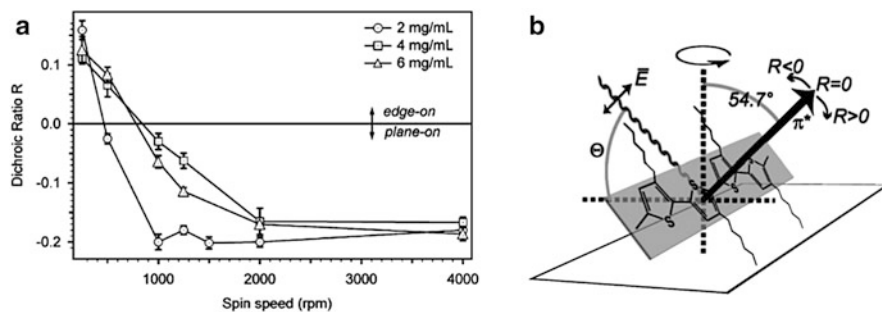


Fig. 18 (a) Results obtained by carbon K-edge NEXAFS measurements of P3HT films cast from chloroform for various spin speeds [71]. Positive values of the dichroic ratio R denote an edge-on orientation of the polymer backbone; negative values denote a face-on orientation ("plane-on"). (b) Chain orientation with respect to the substrate, with the π^* -transition being perpendicular to the conjugated backbone. (Reprinted with permission from Delongchamp et al. [71]. Copyright (2005) American Chemical Society)

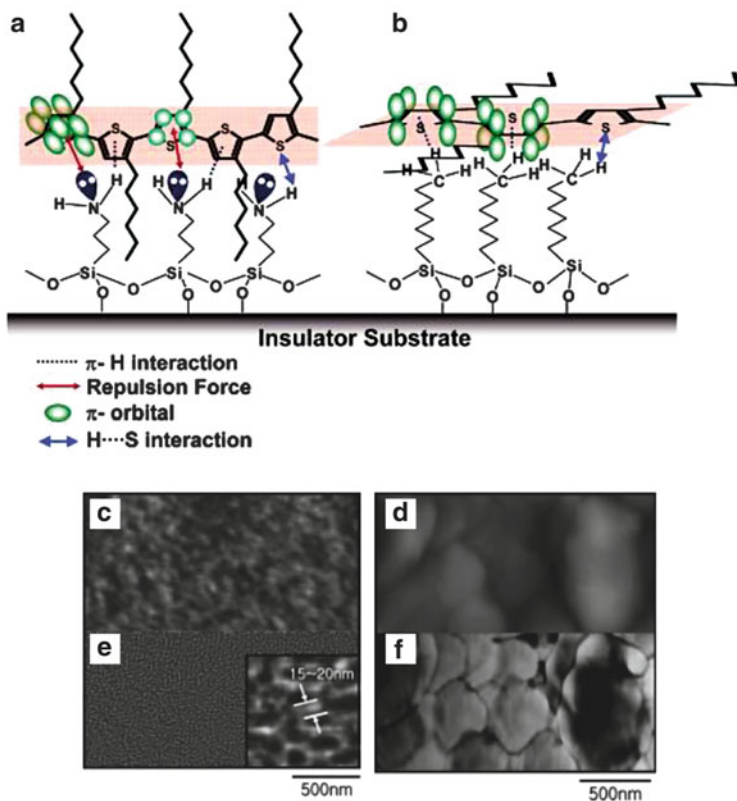


Fig. 19 Molecular orientation of P3HT on different surfaces with (a) edge-on and (b) face-on orientation [105]. (c) Height and (e) phase AFM images of P3HT on a NH_2 -terminated SAM. (d) Height and (f) phase AFM images of P3HT on a CH_3 -terminated SAM [104]. (Reprinted with permission from Kim et al. [105]. Copyright (2005) American Chemical Society. And reprinted with permission from Kim et al. [104]. (Copyright (2005) Wiley-VCH)

monolayer on substrates treated with octyltrichlorosilane [104, 105]. Figure 19 illustrates the variation in molecular orientation for different surfaces obtained by SAMs of different end-group functionalization. Thereby, the change in chain orientation is attributed to different interfacial interactions.

It should be noted that the orientation of the chains with respect to the substrate is not uniform throughout the film and is highly sensitive to the film thickness [103, 106]. For thick films in the range of a few hundreds of nanometers, π -stacked aggregates are randomly oriented and distributed in an amorphous matrix, whereas a preferential alignment of the chains is reported if the film thickness is in the range of the crystal size, i.e., below 25 nm. This is explained by a preferential pinning of the chains at the film–substrate interface, which results in a high degree of edge-on orientation in the first few layers of the film.

4.2 *Inducing Order and Orientation in P3HT Thin Films*

Due to the structural complexity of semicrystalline polymers such as P3HT, charge transport bottlenecks are difficult to determine. As opposed to small molecules, crystalline grains in conjugated polymers are usually too small to allow device fabrication within a single grain or across a single, isolated grain boundary. Therefore, typical macroscopic transport measurements based on field-effect transistors, for instance, average over a great number of randomly oriented crystals and grain boundaries. It remains extremely challenging to measure the impact of the structural anisotropy within a crystalline grain as well as the influence of grain boundaries of different orientation on charge transport. The main approach for overcoming this problem is to induce high in-plane orientation in thin polymer films. These highly anisotropic layers can serve as a tool for the study of optical and electronic properties along different structural and crystallographic directions. In addition, the introduction of controlled defects enables the probing of the impact of specific morphological features.

There are different approaches to the synthesis of highly ordered, anisotropic films. For homogeneous layers, anisotropy is mainly induced by controlling nucleation and growth processes and by methods based on shearing forces such as mechanical rubbing. In patterned thin films, confinement-induced orientation is exploited to obtain structural anisotropy. In the following section, different ideas on achieving structural anisotropy for homogeneous and patterned polymer layers and its impact on charge transport is discussed.

4.2.1 *Order in Homogeneous Thin Films*

Control of Nucleation and Growth

Epitaxial Crystallization

Epitaxial crystallization on orienting surfaces as one elegant method to induce order is thoroughly described by Brinkmann et al. [45]. We briefly highlight the main findings regarding the charge transport anisotropy of such films. Following the approach of directional epitaxial crystallization (DEC) adjusted by Brinkmann and Wittmann [107] and De Rosa et al. [108], Jimison et al. produced highly anisotropic layers of P3HT with fiber-like morphology after directional solidification on the crystallizable solvent 1,3,5-trichlorobenzene (TCB) (see Fig. 20) [19]. Thereby, the polymer backbone (c_{P3HT}) orients parallel to the long axis of the TCB needles (c_{TCB}), with the majority of chains adopting a face-on orientation (Fig. 20d). Transistor measurements in the a - c -plane of these anisotropic layers revealed a low charge transport barrier at grain boundaries parallel to the fiber axis compared with fiber-to-fiber grain boundaries. This result is explained by the relative grain orientation. Grain boundaries along the fiber separate crystallites in which all the chains orient along the fiber axis. In this geometry, it is likely that straight intergrain

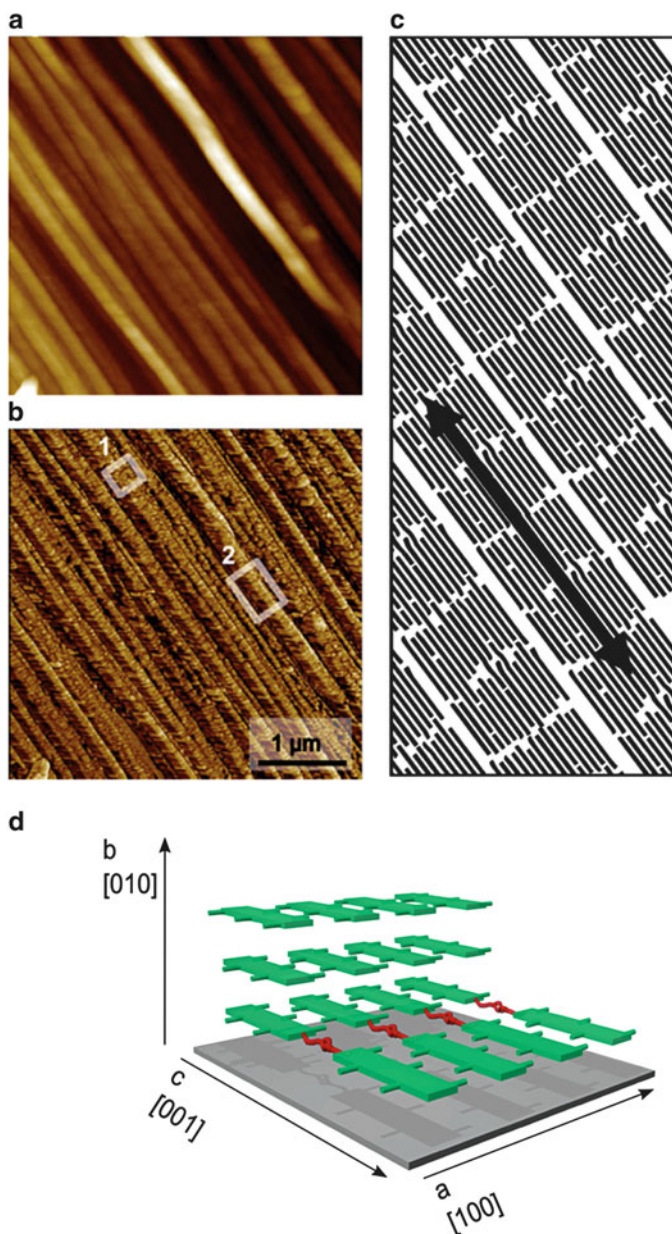


Fig. 20 AFM height (a) and phase (b) images of P3HT oriented via epitaxial directional crystallization [19]. A domain of equiaxed crystallites is highlighted in *box 1*, and a domain of elongated crystallites is marked by *box 2*. (c) Chain alignment within the fibers, with the chain axis being indicated by the *black arrow*. (d) Predominant face-on texture within the oriented fibers, allowing for charge transport measurements in the *a-c*-plane. (Reprinted with permission from Jimison et al. [19]. Copyright (2009) Wiley-VCH)

chains bridge the boundary and provide efficient charge transport pathways between crystalline grains in the fiber direction (see discussion on the concept of tie molecules in Sect. 4.1.2). By contrast, fiber-to-fiber grain boundaries only allow for intergrain chains with sharp bends and twists, which hamper charge transport. Charge transport along the fiber axis is around one order of magnitude higher than in the perpendicular direction.

Spherulite Growth

The order of P3HT thin films can be further realized via low nucleation densities obtained by controlled homogeneous nucleation and self-seeding. Conventional deposition techniques such as spin-coating usually result in a random orientation of the crystalline lamellae due to the high and uncontrolled nucleation. Spherulitic structures of classical, semicrystalline polymers such as polyethylene with low nucleation density are typically generated from the melt. However, melt-annealing of conjugated polymers is problematic due to the high melting temperatures and potential thermal degradation. Although spherulites for P3AT have not been observed after spin-coating and melt-annealing, Lu et al. and our group reported the formation of P3AT spherulites by solvent vapor annealing [20, 109–111]. Lu et al. reported on the transition of form I to form II in poly(3-butylthiophene)s associated with spherulite formation when thin films were treated with CS₂ vapor [110, 111]. A precise control of nucleation density and, hence, spherulite size for P3HT was achieved by us by introducing an approach based on the controlled swelling and subsequent deswelling in CS₂ vapor of well-defined pressure [20, 109]. Nucleation densities much smaller than those obtained after typical spin-casting conditions were achieved, resulting in spherulitic structures of 10–100 μm in diameter (see Fig. 21a). Thereby, the lamellar crystals composed of highly ordered, edge-on oriented chains exhibited common in-plane alignment over several tens of micrometers. Starting from a pre-cast film, swelling in solvent vapor atmosphere of sufficient pressure results in a complete dissolution of P3HT crystals present in the film after spin-coating. In this solution-like state, isolated chains adopt a flexible coil configuration that is reflected in a single broad peak at 465 nm in the absorption spectrum (illustrated in Fig. 21b). Recrystallization is induced by a controlled deswelling of the film to form a supersaturated solution, and can be followed in-situ by polarized optical microscopy (POM) and UV–vis absorption. Nucleation density is adjusted by controlling the degree of supercooling or by self-seeding, the latter approach relying on a small number of nuclei that remain in the solvent-swollen film and act as seeds in subsequent recrystallization. Following this methodology, nucleation densities over several orders of magnitude can be realized independently of crystal growth conditions.

By decreasing the nucleation density to such an extent that a single transistor can be placed in an ordered crystalline domain, charge transport measurements in the *b*-*c*-plane could be performed. For bottom gate, bottom contact transistors, average mobilities of $\mu_{\parallel} = 0.07 \text{ cm}^2/\text{V s}$ and $\mu_{\perp} = 0.20 \text{ cm}^2/\text{V s}$ parallel (II) and perpendicular (\perp) to the spherulite growth direction were found, meaning that charge

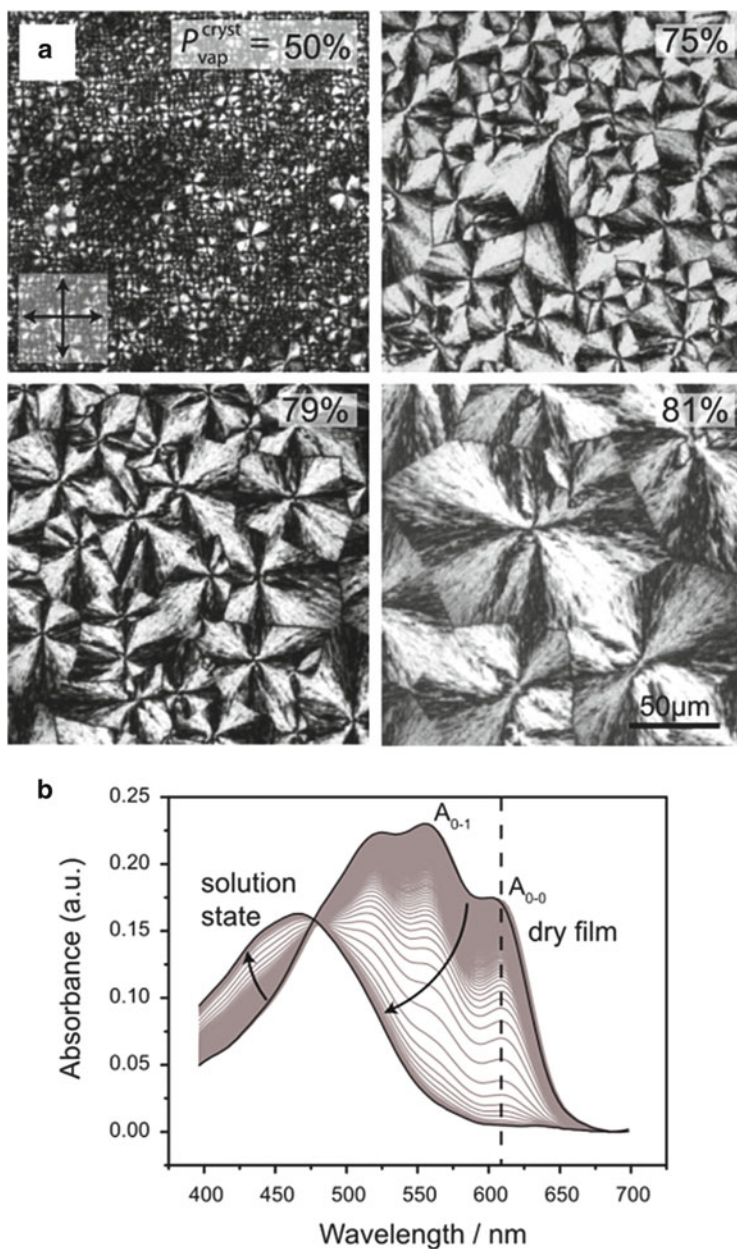


Fig. 21 (a) POM images of P3HT films crystallized at the denoted solvent vapor pressure $P_{\text{vap}}^{\text{cryst}}$ for 30 min after primary swelling at 91% (CS_2 vapor) [109]. (b) In-situ absorption spectra of a P3HT film swollen in 90% CS_2 vapor. (Reprinted with permission from Crossland et al. [109]. Copyright (2011) Wiley-VCH)

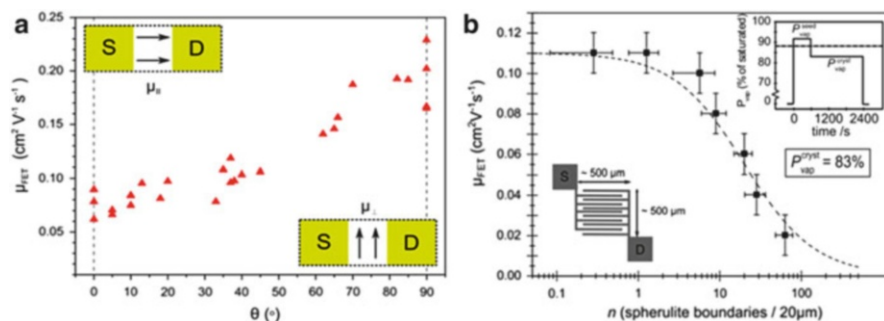


Fig. 22 (a) Mobility μ_{FET} within a spherulite as a function of the angle θ between the charge transport direction and the spherulite growth direction, the latter being equivalent to the π -stacking direction [20]. The insets demonstrate the spherulite growth direction within a transistor channel. (b) μ_{FET} measured in interdigitating transistor channels ($L = 20 \mu\text{m}$, $W = 10 \mu\text{m}$) as a function of the calculated number n of spherulite boundaries per $20 \mu\text{m}$ transistor channel. (Reprinted with permission from Crossland et al. [20]. Copyright (2012) Wiley-VCH.)

transport over macroscopic distances is around three times higher perpendicular to the crystalline lamellae than in π -stacking direction (Fig. 22). We attribute this observation to the presence of tie-molecules that bridge the amorphous regions between quasiparallel lamellae and therefore offer highly efficient transport pathways in the direction of the chain axis, despite the periodic appearance of amorphous zones. In contrast, a clear drop in the field-effect mobility is observed as soon as the number of nonaligned, interspherulite boundaries in the transistor channel exceeds one. There are two potential explanations for this observation: First, macroscopic charge transport might be impeded by a greater width of amorphous material in between adjacent spherulites compared with the amorphous, interlamellar regions within the spherulites. Second, tie-molecules are less likely to bridge nonaligned grain boundaries between adjacent spherulites than low-angle boundaries between quasiparallel lamellae. The latter interpretation (illustrated in Fig. 23) is in accordance with the model of Salleo and coworkers proposing that grain boundaries are not isotropic [112].

Mechanical Rubbing as Shearing Force

Shearing forces can further be used to induce alignment of the initially unoriented polymer chains in the solid state. The advantage of methods based on shearing forces is that they are independent of the applied substrate and, therefore, permit large-scale processing, which is crucial for device manufacture. In this regard, Nagamatsu et al. used the friction transfer method originally introduced by Wittmann and Smith [113] for orienting layers of poly(tetrafluoroethylene)s in order to produce highly anisotropic layers of P3HT [99]. Another method for orienting P3HT is mechanical rubbing, which is extensively used for the orientation

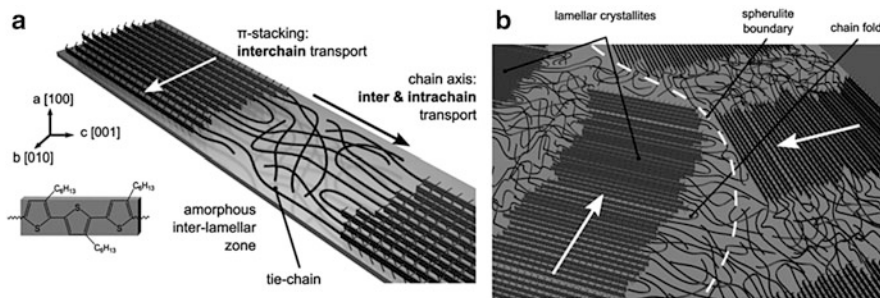


Fig. 23 (a) Quasiparallel lamellae composed of stacked aggregates (*solid rectangles*) that are separated by amorphous domains (*loose lines*) [20]. The chains adopt an edge-on orientation with the alkyl chains pointing normal to the substrate, which allows probing of the charge transport anisotropy in the b - c -plane. (b) Spherulite boundary where ordered domains meet. (Reprinted with permission from Crossland et al. [20]. Copyright (2012) Wiley-VCH)

of polyimide films applied as alignment layers in liquid crystal displays. Brinkmann and coworkers performed a detailed study on the orientation mechanism of P3HT by mechanical rubbing using a combination of TEM and polarized absorption spectroscopy [100]. In rubbed P3HT layers, the polymer backbone orients along the rubbing direction and the chains undergo a transition from edge-on to face-on, which was evidenced by electron diffraction (see Fig. 24a). After solution-casting, the ED pattern consists of a broad ring, which is assigned to the (020) reflection of the π -stacking (0.38 nm), indicating a preferential edge-on texture within isotropically oriented, crystalline domains. Rubbing (one or two cycles) of P3HT results in the appearance of arced ($h00$) reflections on the equator caused by the preferred in-plane orientation of the polymer backbone parallel to the rubbing direction. After four rubbing cycles, the (020) reflection is almost completely absent, while strongly arced ($h00$) reflections with $h = 1, 2, 3$ define the ED pattern. This observation demonstrates two points: (1) the degree of in-plane alignment of the polymer backbone parallel to the rubbing increases with increasing number of rubbing cycles and (2) rubbing causes the chains to undergo a transition from edge-on to face-on. Polarized absorption further confirms the optical anisotropy of rubbed layers of P3HT, estimated by the dichroic ratio at 550 nm (Fig. 24b). The degree of in-plane alignment is highly dependent on the molecular weight of the used sample, with the maximum alignment achieved for low molecular weights (Fig. 24c). This result is attributed to the presence of entanglements and chain folds for high molecular weight P3HT that impede chain reorientation and alignment of the pre-aggregated π -stacks. The effect of high temperature rubbing is currently being explored by Brinkmann and coworkers. The evolution of structural anisotropy as a function of molecular weight is reflected in a significant charge transport anisotropy in the a - c -plane, which is greatly increased for short chains of $M_w < 10$ kg/mol. Thereby, charge transport along the polymer chains is more than one order of magnitude higher than along the insulating side chains. This

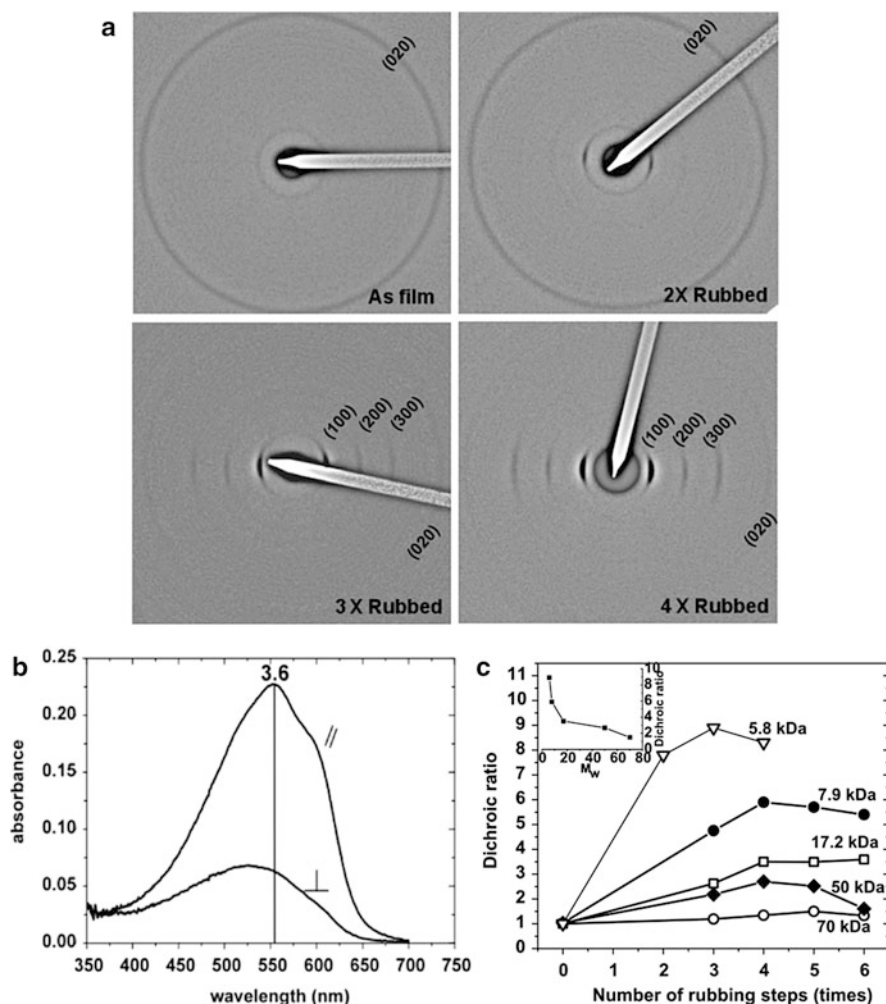


Fig. 24 (a) ED pattern of as-cast and rubbed layers of P3HT ($M_w = 17.2$ kg/mol) with increasing number of rubbing cycles [100]. For all patterns, the rubbing direction is oriented in the vertical direction. Each rubbing step is defined by a rubbing length of $l = 50$ cm. (b) Polarized absorption spectrum of a rubbed layer of P3HT ($M_w = 17.2$ kg/mol). The incident light is polarized parallel (II) and perpendicular (\perp) to the rubbing direction. (c) Evolution of the dichroic ratio measured at 550 nm as function of number of rubbing steps for different molecular weights ranging from 5.8 to 70 kg/mol. The inset displays the highest dichroic ratio measured for rubbed layers of P3HT of different molecular weight. (Reprinted with permission from Hartmann et al. [100]. Copyright (2011) Wiley-VCH)

observation is in agreement with results obtained by Heil et al., who focused on transistor measurements in rubbed layers of P3HT [114].

4.2.2 Order in Patterned Thin Films

Besides chain orientation, the shape of micro- and nanostructures plays a crucial role in device performance. For instance, bulk-heterojunction organic solar cells require phase separation of the donor and acceptor on the nanometer length scale in order to allow for efficient exciton separation into free charges. Within these phase-separated functional layers, charge transport to the respective electrodes is highly affected by both crystallinity and chain orientation. For applications, it is therefore essential to gain control of both the shape of nanostructures and the chain orientation within the nanostructures. Patterning of polymer layers in micro- or nanometer-sized structures is mainly achieved by lithographic methods, particularly nanoimprint lithography (NIL). In the standard NIL process, a rigid mold with nanostructured features is pressed into the polymer film at high pressure and enhanced temperature (above the glass transition temperature of the polymer). The mold is removed after cooling of the film below the T_g . The mechanism of chain orientation within confined geometries is complex and, according to Hu and Jonas, different factors must be considered [115]: reduced nucleation probability within cavities, graphoepitaxial alignment, rheological orientation, confinement, and pressure during the patterning process. It is not yet fully understood how each parameter affects a specific material.

NIL-induced orientation was first found for polyvinylidene fluoride (PVDF) and the liquid crystalline polymer poly(9,9-dioctylfluorene-*co*-benzothiadiazole) (F8BT) [116–118]. Structural anisotropy was also reported for P3HT after patterning by NIL. For instance, Cui et al. described strong optical birefringence for gratings of P3HT (700 nm periodicity) produced by NIL, most probably the result of stretching of chains in amorphous domains and reorientation of microcrystals [119]. A detailed investigation of the molecular orientation in nanostructures via GIXRD was given by Hu and coworkers and Ocko and coworkers [97, 120]. Hu and coworkers found that the molecular orientation is highly sensitive to the geometry of the nanostructures achieved via NIL. For both nanopillars and nanogratings, a vertical alignment of the backbone is found because the polymer chains orient along the flow during the imprinting process (see Fig. 25) [97]. In P3HT nanogratings, the π -stacking direction points along the grating axis. The orientation mechanism is explained by a combination of flow-induced chain alignment, attractive π - π interactions between neighboring chains, and hydrophobic interactions between the alkyl chains and the SAM-treated mold surface. By contrast, Ocko and coworkers reported a face-on orientation of chains in nanogrooves produced by NIL, while the polymer backbone preferentially aligns along the groove axis [120]. The variance of these results illustrates the importance of the mold geometry comprising the width and height of the nanostructures as well as the thickness of the residual layer, all parameters having a significant impact on the flow of material

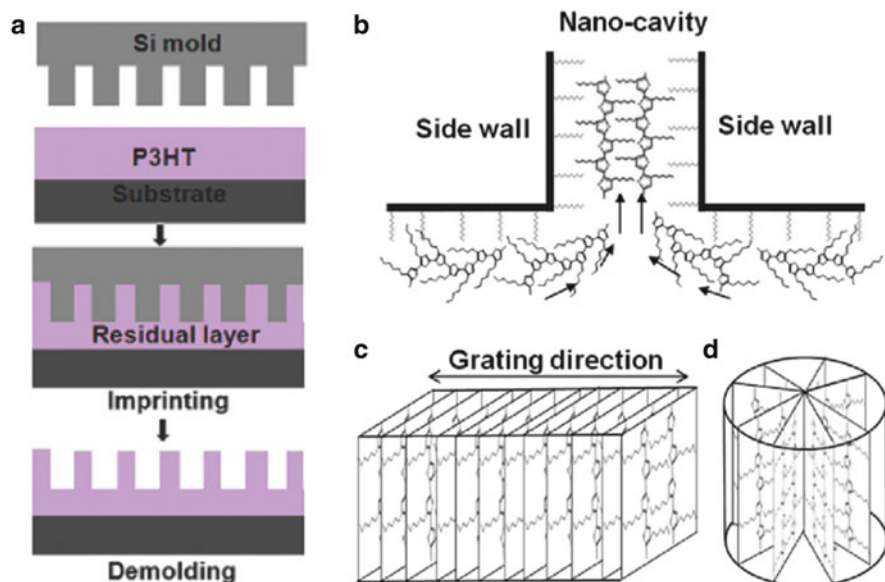


Fig. 25 Vertical chain alignment of P3HT within nanostructures produced by nanoimprint lithography (NIL) [97]: (a) the nanoimprinting process; (b) the chain alignment process induced by NIL, caused by both the material flow and interactions between the alkyl chains of the polymer chain and the hydrophobic surface of the mold cavities; and (c, d) ideal chain orientation within molds of different geometry, namely nanogratings (c) and nanopillars (d). (Reprinted with permission from Aryal et al. [97]. Copyright (2009) American Chemical Society)

during the imprinting process. On the basis of these results, Hu and coworkers proposed a more vertical orientation of chains in the case of high nanostructures with high aspect ratio, whereas the tendency of lying chains (face-on or edge-on) is stronger in flat nanostructures with a relatively thick residual layer [121]. This explanation is in agreement with results by McGehee and coworkers, who observed a clear correlation of structure size and molecular orientation in P3HT pillars of different diameter that were produced by filling anodic alumina films of different pore size with P3HT [122].

A development in NIL is the use of solvent vapor instead of temperature to assist lithography [123–125]. In solvent vapor, the viscosity of the polymer layer is significantly decreased, allowing the patterning of thermosensitive polymers at reduced pressures and temperatures. Line patterns of P3HT achieved by solvent vapor-assisted imprint lithography showed strong birefringence when crystallized under low nucleation density conditions in a well-defined solvent vapor atmosphere, as can be seen in Fig. 26a, b. The AFM image of a single P3HT line of around 500 nm in width (Fig. 26c) reveals a lamellar morphology that is indicative of a predominant edge-on texture, while the lamellae preferentially align parallel to the channel axis.

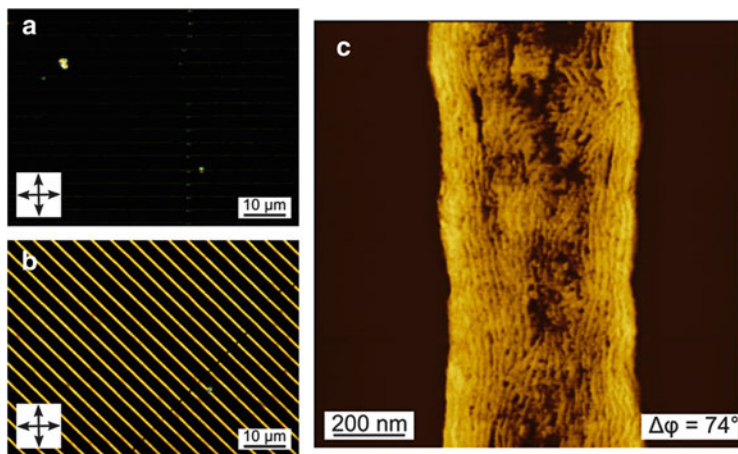


Fig. 26 Oriented films of P3HT prepared by solvent vapor-assisted nanoimprint lithography in a defined CS_2 atmosphere under low nucleation density conditions. (a, b) POM images of a P3HT line pattern with a periodicity of $3\ \mu\text{m}$ showing strong optical birefringence in 0° (a) and 45° (b) orientation with respect to the crossed polarizers. (c) AFM phase image of a single P3HT line, showing confinement-induced orientation of the nanocrystalline lamellae along the channel axis

Nanostructured P3HT films with uniform molecular orientation show great potential for device application. Hu and coworkers reported the manufacture of OFETs and solar cells on the basis of P3HT nanogratings and observed enhanced device performance as a result of 3D chain alignment in the nanogratings [126]. For π -stacking along the grating and a vertical chain orientation [97], in-plane charge transport in OFETs is greatly enhanced along the grating direction and hence along the π -stacking (*b*-axis). Charge carrier mobilities of more than two orders of magnitude lower are found in the perpendicular direction (i.e., side chain direction, *a*-axis), demonstrating a significant charge transport anisotropy in the *a*-*b*-plane. Improved power conversion efficiencies for solar cells based on PCBM and P3HT nanogratings were found compared with bilayer and blend devices of the same material, which further depicts the increased order and interfacial area in the highly ordered P3HT nanostructures. Promising results have also been achieved for patterned solar cells prepared by solvent vapor-assisted imprint lithography [127–129].

Despite the power of NIL, there are further methods for obtaining highly ordered micro- or nanostructures. For example, we made use of a combination of template-directed dewetting and solvent vapor annealing to produce micrometer-sized P3HT structures of high order (Fig. 27) [130]. At first, solvent vapor-induced dewetting from topographically and chemically patterned transistor substrates allowed confining a fluid P3HT film into the micrometer-sized channels of a transistor. Recrystallization in confinement in controlled solvent vapor atmosphere permits low nucleation densities, leading to the oriented growth of the crystalline lamellae along the confining channel walls (see case A in Fig. 27). In this molecular

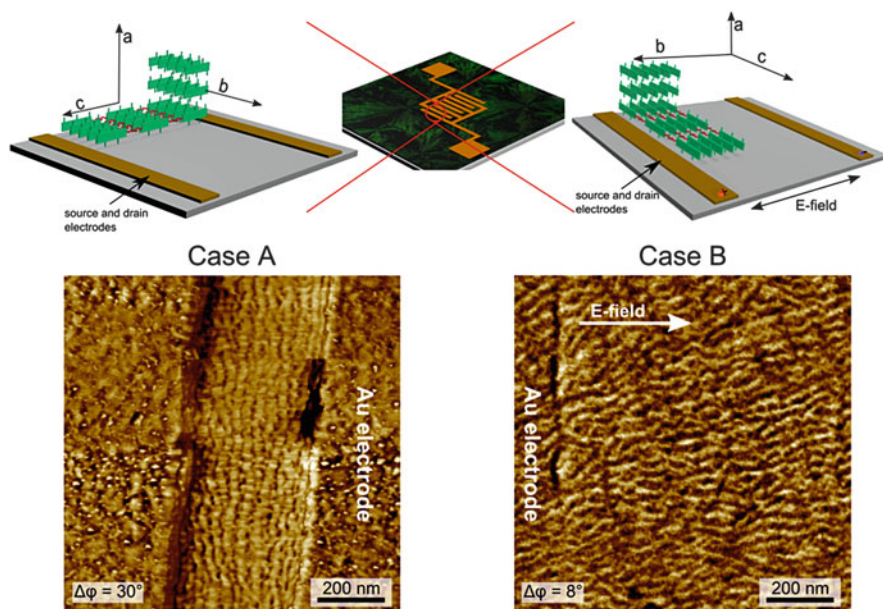


Fig. 27 Controlled dewetting process leading to highly ordered lamellae in edge-on orientation within the channels of a transistor [130]. Thereby, two different orientations of the lamellae with respect to the electrodes are obtained. P3HT films spin-coated on SAM-treated transistor substrates serve as initial state for the experiment. Solvent vapor annealing allows dewetting and subsequent recrystallization in confined structures. *Case A* and *B* demonstrate the molecular orientation within the channels for crystallization without and with applying an electric field between the source and drain electrodes, respectively. The corresponding AFM phase images shown below illustrate the in-plane alignment of the lamellae. (Reprinted with permission from Fischer et al. [130]. Copyright (2012) Royal Society of Chemistry)

orientation, charge transport between the confining electrodes is measured in the chain direction. In contrast, by applying an AC electric field between the confining electrodes during recrystallization, the crystalline lamellae are forced to align along the electric field lines. Here, charge transport measurements probe the mobility along the π -stacking direction (see case B in Fig. 27). Transistor measurements of these two different orientations illustrated in Fig. 27 revealed anisotropic charge transport in the b - c -plane only for high molecular weight P3HT ($M_w = 58.8$ kg/mol) with broad distribution ($PDI = 1.9$), with higher mobilities perpendicular to the lamellae axis and hence in the chain direction. In the case of lower molecular weights and PDIs ($M_w = 30.0$ kg/mol, $PDI = 1.2$), no charge transport anisotropy was detected. We assume that the existence of tie-molecules is less likely and, therefore, charge transport across interlamellar, amorphous domains is impeded by the necessity of intermolecular charge transfer.

5 Conclusions

It is well established that the molecular packing and mesoscale morphology of P3HT thin films play crucial roles in charge transport and device performance. However, due to the complex microstructure of P3HT, comprising a network of crystalline and amorphous domains, systematic investigation of the electrical bottlenecks remains challenging. Besides the molecular orientation, the mesoscale morphology is essential for charge transport, which is a complex multiscale process. Hence, different length scales must be considered. On a molecular scale, the charge carrier mobility is affected by intramolecular and intermolecular charge transport. The former is highly sensitive to the conformation of the chain and, hence, to potential defects along the backbone that reduce the conjugation length. The latter is defined by the strength of π – π interactions between adjacent chains. On a macroscopic scale, the charge transport is determined by the interconnectivity of the crystalline domains that are embedded in amorphous material. The introduction of order and orientation in P3HT thin films over large surface areas allows a better understanding of charge transport along different crystallographic directions and, hence, charge transport bottlenecks can be identified.

To summarize, the control and understanding of morphology from the molecular to the macroscopic scale is crucial for optical and electrical properties and therefore also for device applications. P3HT, which has been the working horse of the polymer electronic community for many years, can be regarded as a model semi-crystalline polymer for more complicated, but also more efficient, polymers based on other repeating units, e.g., donor–acceptor polymers.

Acknowledgements Financial support is acknowledged from the DFG within IRTG-1642, SPP1355 and the Emmy Noether Programme. We thank F. Fischer, Dr. A. Ruff and M. Goll from our group for support with Figures 2, 13 and 16.

References

1. Sirringhaus H, Brown PJ, Friend RH, Nielsen MM, Bechgaard K, Langeveld-Voss BMW, Spiering AJH, Janssen RAJ, Meijer EW, Herwig P, de Leeuw DM (1999) *Nature* 401:685–688
2. Sirringhaus H, Kawase T, Friend RH, Shimoda T, Inbasekaran M, Wu W, Woo EP (2000) *Science* 290:2123–2126
3. Yan H, Chen Z, Zheng Y, Newman C, Quinn JR, Dötz F, Kastler M, Facchetti A (2009) *Nature* 457:679–686
4. He Z, Zhong C, Su S, Xu M, Wu H, Cao Y (2012) *Nat Photon* 6:591–595
5. Bao Z, Dodabalapur A, Lovinger AJ (1996) *Appl Phys Lett* 69:4108–4110
6. Spano FC (2005) *J Chem Phys* 122:234701
7. Kim Y, Cook S, Tuladhar SM, Choulis SA, Nelson J, Durrant JR, Bradley DDC, Giles M, McCulloch I, Ha C-S, Ree M (2006) *Nat Mater* 5:197–203
8. Salleo A (2007) *Mater Today* 10:38–45
9. Muthukumar M (2000) *Eur Phys J E* 3:199–202

10. Muthukumar M (2007) Shifting paradigms in polymer crystallization. In: Reiter G, Strobl GR (eds) Progress in understanding of polymer crystallization. Springer, Berlin/Heidelberg, p 1–18
11. Phillips PJ (1968) Rep Prog Phys 53:549–604
12. Keller A, Machin MJ (1967) J Macromol Sci B Phys 1:41–91
13. Brady JM, Thomas EL (1989) J Mater Sci 24:3311–3318
14. Till PH (1957) J Polym Sci 24:301–306
15. Young R, Bowden P (1973) J Mater Sci 8:1177–1184
16. Wu Z, Petzold A, Henze T, Thurn-Albrecht T, Lohwasser RH, Sommer M, Thelakkat M (2010) Macromolecules 43:4646–4653
17. Zen A, Pflaum J, Hirschmann S, Zhuang W, Jaiser F, Asawapirom U, Rabe JP, Scherf U, Neher D (2004) Adv Funct Mater 14:757–764
18. Kline RJ, McGehee MD, Kadnikova EN, Liu J, Fréchet JMJ, Toney MF (2005) Macromolecules 38:3312–3319
19. Jimison LH, Toney MF, McCulloch I, Heeney M, Salleo A (2009) Adv Mater 21:1568–1572
20. Crossland EJW, Tremel K, Fischer F, Rahimi K, Reiter G, Steiner U, Ludwigs S (2012) Adv Mater 24:839–844
21. Lin JW-P, Dudek LP (1980) J Polym Sci Polym Chem Ed 18:2869–2873
22. Yamamoto T, Sanechika K, Yamamoto A (2008) J Polym Sci Polym Lett Ed 18:2869–2873
23. McCullough RD, Lowe RD (1992) J Chem Soc Chem Commun 1992(1):70–72
24. McCullough RD, Lowe RD, Jayaraman M, Anderson DL (1993) J Org Chem 58:904–912
25. Chen T-A, Rieke RD (1992) J Am Chem Soc 114:10087–10088
26. Loewe RS, Khersonsky SM, McCullough RD (1999) Adv Mater 11:250–253
27. Senkovskyy V, Khanduyeva N, Komber H, Oertel U, Stamm M, Kuckling D, Kiriy A (2007) J Am Chem Soc 129:6626–6632
28. Bronstein HA, Luscombe CK (2009) J Am Chem Soc 131:12894–12895
29. Sista P, Luscombe CK (2014) Progress in the synthesis of poly(3-hexylthiophene). (2014) Adv Polym Sci. doi:[10.1007/12_2014_278](https://doi.org/10.1007/12_2014_278)
30. Trznadel M, Pron A, Zagorska M, Chrzaszcz R, Pielichowski J (1998) Macromolecules 31:5051–5058
31. Gritzner G, Kuta J (1984) Electrochim Acta 29:869–873
32. Skompska M, Szkurlat A (2001) Electrochim Acta 46:4007–4015
33. Heinze J, Frontana-Uribe BA, Ludwigs S (2010) Chem Rev 110:4724–4771
34. Cardona CM, Li W, Kaifer AE, Stockdale D, Bazan GC (2011) Adv Mater 23:2367–2371
35. Pommerehne J, Vestweber H, Guss W, Mahrt RF, Bässler H, Porsch M, Daub J (1995) Adv Mater 7:551–554
36. Scharber MC, Mühlbacher D, Koppe M, Denk P, Waldauf C, Heeger AJ, Brabec CJ (2006) Adv Mater 18:789–794
37. Guan Z-L, Kim JB, Wang H, Jaye C, Fischer DA, Loo Y-L, Kahn A (2010) Org Electron 11:1779–1785
38. Heffner GW, Pearson DS (1991) Macromolecules 24:6295–6299
39. Adachi T, Bazard J, Ono RJ, Hanson B, Traub MC, Wu Z-Q, Li Z, Bolinger JC, Ganesan V, Bielawski CW, Vanden Bout DA, Barbara PF (2011) J Phys Chem Lett 2:1400–1404
40. Chen T, Wu X, Rieke RD (1995) J Am Chem Soc 117:233–244
41. Mao H, Xu B, Holdcroft S (1993) Macromolecules 26:1163–1169
42. Xu B, Holdcroft S (1993) Macromolecules 26:4457–4460
43. Kim DH, Han JT, Park YD, Jang Y, Cho JH, Hwang M, Cho K (2006) Adv Mater 18:719–723
44. Rahimi K, Botiz I, Stingelin N, Kayunkid N, Sommer M, Koch FPV, Nguyen H, Couembier O, Dubois P, Brinkmann M, Reiter G (2012) Angew Chem Int Ed 51:11131–11135
45. Brinkmann M, Hartmann L, Kayunkid N, Djurado D (2014) Understanding the structure and crystallization of regioregular poly(3-hexylthiophene) from the perspective of epitaxy. Adv Polym Sci. doi:[10.1007/12_2014_280](https://doi.org/10.1007/12_2014_280)

46. Lim JA, Liu F, Ferdous S, Muthukumar M, Briseno AL (2010) *Mater Today* 13:14–24
47. Ihn KJ, Moulton J, Smith P (1993) *J Polym Sci B Polym Phys* 31:735–742
48. Samitsu S, Shimomura T, Heike S, Hashizume T, Ito K (2008) *Macromolecules* 41:8000–8010
49. Liu J, Arif M, Zou J, Khondaker SI, Zhai L (2009) *Macromolecules* 42:9390–9393
50. Berson S, De Bettignies R, Bailly S, Guillerez S (2007) *Adv Funct Mater* 17:1377–1384
51. Koppe M, Brabec CJ, Heiml S, Schausberger A, Duffy W, Heeney M, McCulloch I (2009) *Macromolecules* 42:4661–4666
52. Sun S, Salim T, Wong LH, Foo YL, Boey F, Lam YM (2011) *J Mater Chem* 21:377–386
53. Oosterbaan WD, Bolsée J-C, Gadisa A, Vrindts V, Bertho S, D’Haen J, Cleij TJ, Lutsen L, McNeill CR, Thomsen L, Manca JV, Vanderzande D (2010) *Adv Funct Mater* 20:792–802
54. Kiriy N, Jähne E, Adler H-J, Schneider M, Kiriy A, Gorodyska G, Minko S, Jehnichen D, Simon P, Fokin AA, Stamm M (2003) *Nano Lett* 3:707–712
55. Li L, Lu G, Yang X (2008) *J Mater Chem* 18:1984–1990
56. Park YD, Lee HS, Choi YJ, Kwak D, Cho JH, Lee S, Cho K (2009) *Adv Funct Mater* 19:1200–1206
57. Kim B, Kim M, Kim J (2010) *ASC Nano* 4:2160–2166
58. Malik S, Jana T, Nandi AK (2001) *Macromolecules* 34:275–282
59. Malik S, Nandi AK (2007) *J Appl Polym Sci* 103:2528–2537
60. Merlo JA, Frisbie CD (2003) *J Polym Sci B Polym Phys* 41:2674–2680
61. Merlo JA, Frisbie CD (2004) *J Phys Chem B* 108:19169–19179
62. Mas-Torrent M, Den Boer D, Durkut M, Hadley P, Schenning APHJ (2004) *Nanotechnology* 15:S265–S269
63. Samitsu S, Shimomura T, Heike S, Hashizume T, Ito K (2010) *Macromolecules* 43:7891–7894
64. Xin H, Kim FS, Jenekhe SA (2008) *J Am Chem Soc* 130:5424–5425
65. Xin H, Ren G, Kim FS, Jenekhe SA (2008) *Chem Mater* 20:6199–6207
66. Kim JS, Lee JH, Park JH, Shim C, Sim M, Cho K (2011) *Adv Funct Mater* 21:480–486
67. Yang H, Shin TJ, Yang L, Cho K, Ryu CY, Bao Z (2005) *Adv Funct Mater* 15:671–676
68. Yang H, LeFevre SW, Ryu CY, Bao Z (2007) *Appl Phys Lett* 90:172116
69. Chang J-F, Sun B, Breiby DW, Nielsen MM, Sölling TI, Giles M, McCulloch I, Sirringhaus H (2004) *Chem Mater* 16:4772–4776
70. Wang G, Swensen J, Moses D, Heeger AJ (2003) *J Appl Phys* 93:6137
71. Delongchamp DM, Vogel BM, Jung Y, Gurau MC, Richter CA, Kirillov OA, Obrzut J, Fischer DA, Sambasivan S, Richter LJ, Lin EK (2005) *Chem Mater* 17:5610–5612
72. Kline RJ, McGehee MD, Toney MF (2006) *Nat Mater* 5:222–228
73. Kline RJ, McGehee MD, Kadnikova EN, Liu J, Fréchet MJM (2003) *Adv Mater* 15:1519–1522
74. Zen A, Saphiannikova M, Neher D, Grenzer J, Grigorian S, Pietsch U, Asawapirom U, Janietz S, Scherf U, Lieberwirth I, Wegner G (2006) *Macromolecules* 39:2162–2171
75. Verilhac J-M, LeBlevenec G, Djurado D, Rieutord F, Chouiki M, Travers J-P, Pron A (2006) *Synth Met* 156:815–823
76. Brown P, Thomas D, Köhler A, Wilson J, Kim J-S, Ramsdale C, Sirringhaus H, Friend R (2003) *Phys Rev B* 67:064203
77. Clark J, Silva C, Friend R, Spano F (2007) *Phys Rev Lett* 98:206406
78. Clark J, Chang J-F, Spano FC, Friend RH, Silva C (2009) *Appl Phys Lett* 94:163306
79. Zhang R, Li B, Iovu MC, Jeffries-El M, Sauv   G, Cooper J, Jia S, Tristram-Nagle S, Smilgies DM, Lambeth DN, McCullough RD, Kowalewski T (2006) *J Am Chem Soc* 128:3480–3481
80. Yang H, Shin TJ, Bao Z, Ryu CY (2007) *J Polym Sci B Polym Phys* 45:1303–1312
81. Pascui OF, Lohwasser R, Sommer M, Thelakkat M, Thurn-Albrecht T, Saalw  chter K (2010) *Macromolecules* 43:9401–9410
82. Mena-Osteritz E (2002) *Adv Mater* 14:609–616
83. Gr  vin B, Rannou P, Payerne R, Pron A, Travers J-P (2003) *Adv Mater* 15:881–884

84. Noriega R, Rivnay J, Vandewal K, Koch FPV, Stingelin N, Smith P, Toney MF, Salleo A (2013) *Nat Mater* 12:1038–1044
85. Kim DH, Park YD, Jang Y, Kim S, Cho K (2005) *Macromol Rapid Commun* 26:834–839
86. Dang MT, Hirsch L, Wantz G, Wuest JD (2013) *Chem Rev* 113:3734–3765
87. Zaumseil J (2014) P3HT and other polythiophene field-effect transistors. *Adv Polym Sci*. doi:[10.1007/12_2014_279](https://doi.org/10.1007/12_2014_279)
88. Prosa TJ, Winokur MJ, McCullough RD (1996) *Macromolecules* 29:3654–3656
89. Prosa TJ, Winokur MJ, Moulton J, Smith P, Heeger AJ (1992) *Macromolecules* 25:4364–4372
90. Tashiro K, Kobayashi M, Kawai T, Yoshino K (1997) *Polymer* 38:2867–2879
91. Brinkmann M, Rannou P (2007) *Adv Funct Mater* 17:101–108
92. Dudenko D, Kiersnowski A, Shu J, Pisula W, Sebastiani D, Spiess HW, Hansen MR (2012) *Angew Chem* 51:11068–11072
93. Brinkmann M (2011) *J Polym Sci B Polym Phys* 49:1218–1233
94. Malik S, Nandi AK (2002) *J Polym Sci B Polym Phys* 40:2073–2085
95. Snyder CR, Henry JS, DeLongchamp DM (2011) *Macromolecules* 44:7088–7091
96. Lee CS, Dadmun MD (2014) *Polymer* 55:4–7
97. Aryal M, Trivedi K, Hu WW (2009) *ACS Nano* 3:3085–3090
98. Liu J, Sun Y, Gao X, Xing R, Zheng L, Wu S, Geng Y, Han Y (2011) *Langmuir* 27:4212–4219
99. Nagamatsu S, Takashima W, Kaneto K, Yoshida Y, Tanigaki N, Yase K, Omote K (2003) *Macromolecules* 36:5252–5257
100. Hartmann L, Tremel K, Uttiya S, Crossland E, Ludwigs S, Kayunkid N, Vergnat C, Brinkmann M (2011) *Adv Funct Mater* 21:4047–4057
101. Meyerhofer D (1978) *J Appl Phys* 49:3993
102. Aasmundtveit KE, Samuelsen EJ, Guldstein M, Steinsland C, Flornes O, Fagermo C, Seeberg TM, Pettersson LAA, Inganas O, Feidenhansl R, Ferrer S (2000) *Macromolecules* 33:3120–3127
103. Joshi S, Grigorian S, Pietsch U, Pingel P, Zen A, Neher D, Scherf U (2008) *Macromolecules* 41:6800–6808
104. Kim DH, Park YD, Jang Y, Yang H, Kim YH, Han JI, Moon DG, Park S, Chang T, Chang C, Joo M, Ryu CY, Cho K (2005) *Adv Funct Mater* 15:77–82
105. Kim DH, Jang Y, Park YD, Cho K (2005) *Langmuir* 21:3203–3206
106. Joshi S, Pingel P, Grigorian S, Panzner T, Pietsch U, Neher D, Forster M, Scherf U (2009) *Macromolecules* 42:4651–4660
107. Brinkmann M, Wittmann J-C (2006) *Adv Mater* 18:860–863
108. De Rosa C, Park C, Thomas EL, Lotz B (2000) *Nature* 2145:433–437
109. Crossland EJW, Rahimi K, Reiter G, Steiner U, Ludwigs S (2011) *Adv Funct Mater* 21:518–524
110. Lu GH, Li LG, Yang XN (2007) *Adv Mater* 19:3594–3598
111. Lu G, Li L, Yang X (2008) *Macromolecules* 41:2062–2070
112. Street R, Northrup J, Salleo A (2005) *Phys Rev B* 71:165202
113. Wittmann JC, Smith P (1991) *Nature* 352:414–417
114. Heil H, Finnberg T, von Malm N, Schmechel R, von Seggern H (2003) *J Appl Phys* 93:1636
115. Hu Z, Jonas AM (2010) *Soft Matter* 6:21–28
116. Zheng Z, Yim K-H, Saifullah MSM, Welland ME, Friend RH, Kim J-S, Huck WTS (2007) *Nano Lett* 7:987–992
117. Hu Z, Baralia G, Bayot V, Gohy J-F, Jonas AM (2005) *Nano Lett* 5:1738–1743
118. Schmid S, Yim K, Chang M, Zheng Z, Huck W, Friend R, Kim J, Herz L (2008) *Phys Rev B* 77:115338
119. Cui D, Li H, Park H, Cheng X (2008) *J Vac Sci Technol B Microelectron Nanometer Struct* 26:2404

120. Hlaing H, Lu X, Hofmann T, Yager KG, Black CT, Ocko BM (2011) *ACS Nano* 5:7532–7538
121. Yang Y, Mielczarek K, Aryal M, Zakhidov A, Hu W (2012) *ACS Nano* 6:2877–2892
122. Coakley KM, Srinivasan BS, Ziebarth JM, Goh C, Liu Y, McGehee MD (2005) *Adv Funct Mater* 15:1927–1932
123. Voicu NE, Ludwigs S, Crossland EJW, Andrew P, Steiner U (2007) *Adv Mater* 19:757–761
124. Khang D-Y, Lee HH (2000) *Appl Phys Lett* 76:870
125. Lai KL, Hon MH, Leu IC (2011) *J Micromech Microeng* 21:075013
126. Zhou M, Aryal M, Mielczarek K, Zakhidov A, Hu W (2010) *J Vac Sci Technol B Microelectron Nanometer Struct* 28:C6M6
127. He X, Gao F, Tu G, Hasko D, Hüttner S, Steiner U, Greenham NC, Friend RH, Huck WTS (2010) *Nano Lett* 10:1302–1307
128. He X, Gao F, Tu G, Hasko DG, Hüttner S, Greenham NC, Steiner U, Friend RH, Huck WTS (2011) *Adv Funct Mater* 21:139–146
129. Park JY, Hendricks NR, Carter KR (2011) *Langmuir* 27:11251–11258
130. Fischer FSU, Tremel K, Sommer M, Crossland EJC, Ludwigs S (2012) *Nanoscale* 4:2138–2144

P3HT Revisited – From Molecular Scale to Solar Cell
Devices

Ludwigs, S. (Ed.)

2014, VII, 232 p. 105 illus., 65 illus. in color., Hardcover

ISBN: 978-3-662-45144-1